

Isogeometric Least-squares Collocation Method with Consistency and Convergence Analysis

Hongwei Lin^{a,*}, Yunyang Xiong^a, Xiao Wang^a, Qianqian Hu^b

^aDepartment of Mathematics, State Key Lab. of CAD&CG, Zhejiang University, Hangzhou, 310027, China

^bDepartment of Mathematics, Zhejiang Gongshang University, Hangzhou, 310018, China

Abstract

In this paper, we present the isogeometric least-squares collocation (IGA-L) method, which determines the numerical solution by making the approximate differential operator fit the real differential operator in a least-squares sense. The number of collocation points employed in IGA-L can be larger than that of the unknowns. Theoretical analysis and numerical examples presented in this paper show the superiority of IGA-L over state-of-the-art collocation methods. First, a small increase in the number of collocation points in IGA-L leads to a large improvement in the accuracy of its numerical solution. Second, IGA-L method is more flexible and more stable, because the number of collocation points in IGA-L is variable. Third, IGA-L is convergent in some cases of singular parameterization. Moreover, the consistency and convergence analysis are also developed in this paper.

Keywords: Isogeometric analysis, collocation method, least-squares fitting, NURBS, consistency and convergence

1. Introduction

While classical Finite Element Analysis (FEA) methods, widely employed in physical simulations, are based on element-wise piecewise polynomials, computer-aided design (CAD) models are usually represented by non-uniform rational basis splines (NURBSs) with non-linear NURBS basis functions. Therefore, the first task in a CAD model simulation is to transform the non-linear NURBS-represented CAD model into a linear mesh representation. This mesh transformation is a very tedious operation, and it has become the most time-consuming task of the whole FEA procedure. To avoid the mesh transformation and advance the seamless integration of CAD and computer-aided engineering (CAE), isogeometric analysis (IGA) was invented by Hughes et al. [1]. IGA is based on the NURBS basis functions of degree higher than 1, hence it can deal with NURBS-represented CAD models directly. In this way, IGA not only saves a significant amount of computation, it also greatly improves the numerical accuracy of the solution.

In IGA, the analytical solution T to a boundary value problem is approximated by a NURBS function T_r with unknown coefficients. (For brevity, we only mention the boundary value problem in this paper. However, this method is also suitable for the initial value problem.) Solving

*Corresponding author: phone number: 86-571-87951860-8304, fax number: 86-571-88206681, email: hwlin@zju.edu.cn

the boundary value problem is then equivalent to determining the unknown coefficients of T_r . If the order of T_r is higher than that of the differential operator \mathcal{D} of the boundary value problem, $\mathcal{D}T_r$ can be represented explicitly by a NURBS derivative formula. Therefore, collocation methods can be applied to the strong form of the boundary value problem to determine the unknown coefficients of T_r .

In Ref. [2], an isogeometric collocation (IGA-C) method was presented. Suppose n is the number of unknown coefficients of T_r . IGA-C first samples n values $\mathcal{D}T(\eta_j)$, $j = 1, 2, \dots, n$, and then generates a linear system of equations by making $\mathcal{D}T_r$ interpolate the n values, i.e., $\mathcal{D}T_r(\eta_j) = \mathcal{D}T(\eta_j)$, $j = 1, 2, \dots, n$. In this way, the unknown coefficients of T_r can be determined by solving the linear system.

Essentially, IGA-C acquires the unknown coefficients by interpolation, where the number of the collocation points must be equal to that of the unknown coefficients. In this paper, we propose the isogeometric least-squares collocation (IGA-L) method, which allows the number of collocation points to be larger than that of the unknown coefficients. It yields some advantages over IGA-C. Instead of interpolation, IGA-L makes use of approximation to determine the unknown coefficients of T_r . Specifically, IGA-L first samples m values $\mathcal{D}T(\eta_j)$, $j = 1, 2, \dots, m$, where m is greater than the number of unknown coefficients, i.e., $m > n$. The coefficients of the unknown solution T_r are then determined by solving the least-squares fitting problem

$$\min \sum_{j=1}^m \|\mathcal{D}T(\eta_j) - \mathcal{D}T_r(\eta_j)\|^2.$$

There are two advantages of IGA-L over IGA-C. First, numerical tests presented in this paper show that a small increase in the computation of IGA-L leads to a large improvement in the numerical accuracy of the solution, even though the computational cost of IGA-L is only slightly more than that of IGA-C. Second, IGA-L is more flexible and more stable than IGA-C, because IGA-L allows a variable number of collocation points, while the number of collocation points in IGA-C is fixed to be equal to the number of control points.

The structure of this paper is as follows. In Section 1.1, some related work is briefly reviewed. In Section 2, the generic formulation of IGA-L is presented. In Section 3, we show the consistency and convergence properties of IGA-L. After thoroughly comparing IGA-L and IGA-C, both in theory and with numerical examples in Section 4, this paper is concluded in Section 5.

1.1. Related Work

Least-squares collocation methods: Although collocation-based meshless methods are efficient, equilibrium conditions are satisfied only at collocation points. Thus, collocation-based meshless methods can result in significant error. To improve computational accuracy, Zhang et al. developed a least-squares collocation method [3], where equilibrium conditions hold at both collocation points and auxiliary points in a least-squares sense. In order to generate a better conditioned linear algebraic equations, a least-squares meshfree collocation method was proposed, based on first-order differential equations [4]. In Ref. [5], a point collocation method was invented that employs the approximating derivatives based on the moving least-square reproducing kernel approximations. Moreover, several schemes using least-squares collocation methods were developed for two- and three-dimensional heat conduction problems [6], transient and steady-state hyperbolic problems [7], and adaptive analysis problems in linear elasticity [8].

On the other hand, there are some meshfree methods which handle the improvement of stability. By eliminating the rank deficiency with stress points, a meshfree particle method was

developed for large deformation, nonlinear problems that employs a Lagrangian kernel with correction of the derivatives [9]. In [10], a simplified meshfree method for arbitrary evolving cracks was proposed, where the crack is modelled by a discontinuous enrichment that can be arbitrarily aligned in the body at each particle. Moreover, an approach for modelling discrete cracks in meshfree particle methods in three dimension was devised, where the growth of a crack is represented by activation of crack surfaces with arbitrary orientation [11].

However, the consistency and convergence properties of the aforementioned least-squares collocation methods were only validated using numerical examples, and theoretical numerical analyses were not reported. In this paper, we not only develop an isogeometric least-squares collocation method, but also show its consistency and convergence properties in theory.

Isogeometric analysis: NURBS is a mathematical model for representing curves and surfaces by blending weighted control points and NURBS basis functions. Hence, the shape of the NURBS curves and surfaces can be easily modified by moving their control points. Because of the desirable traits of NURBS basis functions, NURBS curves and surfaces have many good properties, such as convex hull, affine invariance, and variation diminishing. Moreover, NURBSs can represent conic sections and quadric surfaces accurately. Therefore, NURBSs have been widely used in CAD, computer-aided manufacturing (CAM), and CAE, and have become a part of numerous industry standards, such as IGES, STEP, ACIS, and PHIGS. For more details on NURBSs, there are excellent books on the subject [12, 13].

While a NURBS employs non-linear basis functions, classical FEA is based on element-wise piecewise polynomials. Hence, when analyzing NURBS-represented CAD models using classical FEA, the CAD model should be discretized into a mesh model. The mesh generation procedure not only yields an approximation, it is also very tedious, and hence has become a bottleneck in FEA. To overcome these difficulties, Hughes et al. invented the IGA technique [1]. Because IGA is based on NURBS basis functions, it can handle NURBS-represented CAD models directly without generating a mesh. Moreover, because NURBSs can represent complex shapes (and physical fields) with significantly fewer control points than a mesh representation, the computational efficiency and numerical accuracy of IGA are higher than the classical FEA method. In addition, because of the knot insertion property of NURBSs, the original shape of the CAD model can be maintained exactly in the refinement procedure [1].

In geometric design, the NURBS representation is usually employed to model curves and surfaces. There are a few effective methods in geometric design for modeling spline solids. To model a NURBS solid for IGA applications, Zhang et al. proposed a solid construction method from a boundary representation [14]. In the study of IGA, making the geometric representation more suitable for analysis purposes is a key research goal. Cohen et al. presented the analysis-aware modeling technique [15]. Moreover, T-spline [16, 17], trimmed surfaces [18], subdivision solids [19], and splines on triangulations [20, 21] were also employed in the IGA method to model the physical domain.

Currently, the IGA method has been successfully applied in various simulation problems, including elasticity [22, 23], structure [24, 25, 26], and fluids [27, 28, 29]. On the other hand, some work concerns the computational aspect of the IGA method, for instance, to improve the accuracy and efficiency by reparameterization and refinement [30, 31, 32, 33, 34]. Moreover, fast solvers for both Galerkin and collocation approaches were developed in Refs. [35, 36].

Isogeometric collocation methods: The collocation method is a simple numerical method for solving differential equations that can generate a solution that satisfies the differential equation at a set of discrete points, called collocation points [37]. If the order of the unknown NURBS function that is employed to approximate the solution of the differential equation is high enough,

the collocation method can be applied to the strong form of the differential equation. In this way, the IGA-C method was presented in Ref. [2]. However, IGA-C is greatly influenced by the collocation points. Recently, a comprehensive study on IGA-C discovered its superior behavior over the Galerkin method in terms of its accuracy-to-computational-time ratio [38], and the consistency and convergence properties of the IGA-C method were developed in Ref. [39]. In Ref. [40], the isogeometric superconvergent collocation method (IGA-SC) was developed, where locations of the collocation points were derived from the superconvergence theory. Furthermore, an optimally convergent isogeometric collocation scheme for odd degrees was proposed in [41], which are a subset of the Galerkin superconvergent points. It was shown that there exist the collocation points, called Cauchy-Galerkin points, that produce the Galerkin solution exactly [42]. In [43], analysis-suitable T-splines were employed in combination with isogeometric collocation methods to solve second- and fourth-order boundary-value problems.

Moreover, based on the local hierarchical refinement of NURBSs, adaptive IGA-Cs were developed and analyzed [38]. Meanwhile, IGA-C has also been extended to multi-patch NURBS configurations, various boundary and patch interface conditions, and explicit dynamic analysis [44]. Recently, IGA-C was successfully employed to solve the Timoshenko beam problem [45] and spatial Timoshenko rod problem [46], showing that mixed collocation schemes are locking-free, independently of the choice of the polynomial degrees for the unknown fields. It was shown that IGA-C is particularly suitable for solving the system of ODEs governing the non-prismatic beam problem [47]. Moreover, IGA-C was proposed for the linear static bending analysis of laminated composite plates governed by Reissner-Mindlin theory [48].

2. Generic Formulation of IGA-L

Consider the following boundary value problem,

$$\begin{cases} \mathcal{D}T = f, & \text{in } \Omega \in \mathbb{R}^d, \\ \mathcal{G}T = g, & \text{on } \partial\Omega, \end{cases} \quad (1)$$

where Ω is the physical domain in \mathbb{R}^d , \mathcal{D} is a differential operator in the physical domain, $\mathcal{G}T = g$ is the boundary condition, and $f : \Omega \rightarrow \mathbb{R}$ and $g : \partial\Omega \rightarrow \mathbb{R}$ are given functions. Suppose d_1 is the maximum order of derivatives appearing in $\mathcal{D} : V \rightarrow W$, where V and W are two Hilbert spaces, and the analytical solution $T \in C^{d_2}(\Omega)$, $d_2 > d_1 \geq 1$.

In IGA, the physical domain Ω is represented by a NURBS mapping:

$$\mathbf{F} : \Omega_0 \rightarrow \Omega, \quad (2)$$

where $\Omega_0 \in \mathbb{R}^d$ is the parametric domain. By replacing the control points of $\mathbf{F}(\Omega_0)$ with unknown control coefficients, the representation of the unknown numerical solution T_r is generated.

Suppose there are n unknown control coefficients in the unknown numerical solution T_r . We first sample m_1 points θ_k inside the parametric domain Ω_0 that correspond to m_1 values $\boldsymbol{\eta}_k = \mathbf{F}(\theta_k)$, $k = 1, 2, \dots, m_1$, inside the physical domain Ω . Furthermore, we sample m_2 points θ_l on the parametric domain boundary $\partial\Omega_0$ that correspond to m_2 values $\boldsymbol{\eta}_l = \mathbf{F}(\theta_l)$, $l = m_1 + 1, m_1 + 2, \dots, m_1 + m_2$, on the physical domain boundary $\partial\Omega$. The total number of these points, i.e., $m = m_1 + m_2$, is greater than the number of unknown coefficients of the numerical solution T_r , namely, $m = m_1 + m_2 > n$. Just as in IGA-C, these sampling points are also called **collocation points**.

Substituting these collocation points into the boundary value problem (1), a system of equations with m equations and n unknowns is obtained (where $m = m_1 + m_2 > n$),

$$\begin{cases} \mathcal{D}T_r(\boldsymbol{\eta}_k) = f(\boldsymbol{\eta}_k), & k = 1, 2, \dots, m_1, \\ \mathcal{G}T_r(\boldsymbol{\eta}_l) = g(\boldsymbol{\eta}_l), & l = m_1 + 1, m_1 + 2, \dots, m_1 + m_2. \end{cases} \quad (3)$$

Arranging the unknowns of the numerical solution T_r into an $n \times 1$ matrix, i.e., $X = [x_1 \ x_2 \ \dots \ x_n]^T$, the system of equations (3) can be represented in matrix form by

$$AX = b.$$

Because the number of equations is greater than the number of unknowns, the solution is sought in the least-squares sense, i.e.,

$$\min_X \|AX - b\|^2. \quad (4)$$

Computation of the least-squares problem (4): The least-squares problem (4) is very important in practice, and there have been developed lots of robust and efficient methods for solving it [49]. One frequently employed method is to solve the normal equation (5),

$$A^TAX = A^Tb. \quad (5)$$

Although the condition number of the matrix A^TA is the square of that of the matrix A , A^TA is a symmetric positive definite matrix, and the normal equation (5) can be solved efficiently by Cholesky decomposition [49]. Moreover, Householder orthogonalization and Given orthogonalization are also two efficient methods [49] which often employed in solving the least-squares problem (4). For more methods on solving (4), please refer to [49].

Remark 1. *We assume that the matrix A is of full rank, and then A^TA is non-singular, and the linear system (5) has unique solution.*

In the following, we will show the consistency and convergence properties of IGA-L, and compare it with IGA-C and IGA-SC [40], both in theory and with numerical examples.

3. Numerical Analysis

In the IGA-L method developed above, a NURBS function T_r is employed to approximate the analytical solution T of the boundary value problem (1), and hence the real differential operator $\mathcal{D}T$ is approximated by $\mathcal{D}T_r$. In Ref. [39], it was shown that both $\mathcal{D}T_r$ and T_r are defined on the same knot intervals, i.e.,

Lemma 1. *If T_r is a NURBS function and \mathcal{D} is a differential operator, then both $\mathcal{D}T_r$ and T_r are defined on the same knot intervals [39].*

Moreover, given a set Φ , the **diameter** of Φ is defined as

$$diam(\Phi) = \max\{d(x, y), x, y \in \Phi\},$$

where $d(x, y)$ is the Euclidean distance between x and y . In the following, we suppose the NURBS function T_r to be defined on a knot grid \mathcal{T}^h , where h is the **knot grid size**: In the one-dimensional

case, \mathcal{T}^h is a knot sequence, and $h = \max_i \{diam([u_i, u_{i+1}])\}$; in the two-dimensional case, \mathcal{T}^h is a rectangular grid, and $h = \max_{i,j} \{diam([u_i, u_{i+1}] \times [v_j, v_{j+1}])\}$; in the three-dimensional case, \mathcal{T}^h is a hexahedral grid, and $h = \max_{i,j,k} \{diam([u_i, u_{i+1}] \times [v_j, v_{j+1}] \times [w_k, w_{k+1}])\}$.

In this section, we study the consistency and convergence properties of IGA-L, i.e., when $h \rightarrow 0$, not only will approximate differential operator \mathcal{DT}_r tend to real operator \mathcal{DT} , but numerical solution T_r will also tend to analytical solution T .

3.1. Consistency

In this section, we explore the consistency property of the IGA-L method. In Section 3.1.1, the consistency of the IGA-L method with special operators which have polynomial coefficients is developed. In Section 3.1.2, the consistency of the IGA-L method in the generic case is studied.

3.1.1. Consistency with special operators

In this section, we deal with special operators \mathcal{D} and \mathcal{G} , which have polynomial coefficients.

Suppose the NURBS function $T_r(\boldsymbol{\eta})$, $\boldsymbol{\eta} \in \Omega_0 \subset \mathbb{R}^d$ defined on the knot grid \mathcal{T}^h , has n unknown control coefficients p_i , i.e.,

$$T_r(\boldsymbol{\eta}) = \sum_i p_i \frac{w_i B_i(\boldsymbol{\eta})}{W(\boldsymbol{\eta})} = \frac{P(\boldsymbol{\eta})}{W(\boldsymbol{\eta})}, \quad \boldsymbol{\eta} = (\eta_1, \eta_2, \dots, \eta_d) \in \Omega_p \subset \mathbb{R}^d, \quad (6)$$

where the subscript i is an index vector, $i = (i_1, i_2, \dots, i_d)$, $w_i > 0$ are known weights,

$$B_i(\boldsymbol{\eta}) = B_{i_1}(\eta_1) B_{i_2}(\eta_2) \cdots B_{i_d}(\eta_d), \quad (7)$$

are the B-spline basis functions. Moreover, the weight function $W(\boldsymbol{\eta})$ is a known polynomial spline function, and $P(\boldsymbol{\eta})$ is a polynomial spline function with n unknown control coefficients p_i .

According to the result developed in Ref. [39], \mathcal{DT}_r can be represented by

$$\mathcal{DT}_r(\boldsymbol{\eta}) = \sum_i p_i \mathcal{D} \frac{w_i B_i(\boldsymbol{\eta})}{W(\boldsymbol{\eta})} = \sum_i p_i \frac{\bar{B}_i(\boldsymbol{\eta})}{\bar{W}(\boldsymbol{\eta})} = \frac{\bar{P}(\boldsymbol{\eta})}{\bar{W}(\boldsymbol{\eta})}, \quad (8)$$

where $\bar{B}_i(\boldsymbol{\eta})$, the result by applying the differential operator \mathcal{D} to $\frac{w_i B_i(\boldsymbol{\eta})}{W(\boldsymbol{\eta})}$, is a polynomial spline function, $\bar{W}(\boldsymbol{\eta}) \neq 0$ is the power of $W(\boldsymbol{\eta})$, and

$$\bar{P}(\boldsymbol{\eta}) = \sum_i p_i \bar{B}_i(\boldsymbol{\eta}), \quad (9)$$

is a polynomial B-spline function with n unknowns p_i .

Similarly, $\mathcal{GT}_r(\boldsymbol{\eta})$ in Eq. (1) can be written as

$$\mathcal{GT}_r(\boldsymbol{\eta}) = \sum_i p_i \mathcal{G} \frac{w_i B_i(\boldsymbol{\eta})}{W(\boldsymbol{\eta})} = \sum_i p_i \frac{\tilde{B}_i(\boldsymbol{\eta})}{\tilde{W}(\boldsymbol{\eta})} = \frac{\tilde{P}(\boldsymbol{\eta})}{\tilde{W}(\boldsymbol{\eta})}, \quad (10)$$

where $\tilde{B}_i(\boldsymbol{\eta})$, the result generated by applying the operator \mathcal{G} to $\frac{w_i B_i(\boldsymbol{\eta})}{W(\boldsymbol{\eta})}$, is a polynomial spline function, $\tilde{W}(\boldsymbol{\eta}) \neq 0$ is a known B-spline function, and

$$\tilde{P}(\boldsymbol{\eta}) = \sum_i p_i \tilde{B}_i(\boldsymbol{\eta}), \quad (11)$$

is an unknown B-spline function with n unknowns p_i .

By the result developed in Ref. [39], $\bar{P}(\boldsymbol{\eta})$ (9) and $\tilde{P}(\boldsymbol{\eta})$ (11) both have the same break point sequence and the same knot intervals as $T_r(\boldsymbol{\eta})$. So they can be made to be defined on the same knot sequence by knot insertion and degree elevation.

Therefore, based on Eqs. (9) and (11), the linear system (3) becomes

$$\begin{cases} \bar{P}(\boldsymbol{\eta}_k) = \sum_i p_i \bar{B}_i(\boldsymbol{\eta}_k) = \bar{W}(\boldsymbol{\eta}_k) f(\boldsymbol{\eta}_k), & k = 0, 1, \dots, m_1, \\ \tilde{P}(\boldsymbol{\eta}_l) = \sum_i p_i \tilde{B}_i(\boldsymbol{\eta}_l) = \tilde{W}(\boldsymbol{\eta}_l) g(\boldsymbol{\eta}_l), & l = m_1 + 1, m_1 + 2, \dots, m_1 + m_2 = m. \end{cases} \quad (12)$$

By Remark 1, the coefficient matrix of the linear system (12) is of full rank. As a consequence, the polynomial spline functions in $\Phi = \{\bar{B}_i(\boldsymbol{\eta}); \tilde{B}_j(\boldsymbol{\eta})\}$ are linear independent. Otherwise, the coefficient matrix of system (12) is not of full rank. Because each of polynomial spline functions in Φ is a linear combination of B-spline basis functions, the spline space generated by the combination of functions in Φ is a B-spline sub-space \mathbb{S} , defined on the knot grid \mathcal{T}^h . Therefore, the least-squares solution to the linear system (12) is actually the least-squares projection to the B-spline sub-space \mathbb{S} . We denote the least-squares projector as \mathcal{P} . Thus, the following lemma is reached.

Lemma 2. *The IGA-L solution to the boundary problem (1) is the least-squares projection to a B-spline sub-space \mathbb{S} .*

In Ref. [50], Shadrin proved the “de Boor’s conjecture”, i.e., the L_∞ -norm of the L_2 -spline projector is bounded independently of the knot sequence in univariate case. Moreover, Passenbrunner et. al. extended this result to tensor product spline projections [51]. That is,

Lemma 3. *Let $\bar{\mathcal{P}} : C(\Omega) \rightarrow \bar{\mathbb{S}}$ is a L_2 projector from the continuous function space $C(\Omega)$ to a B-spline space $\bar{\mathbb{S}}$. There exists a constant $c_{d,k}$, such that,*

$$\|\bar{\mathcal{P}}\|_\infty \leq c_{d,k},$$

where, $c_{d,k}$ is related to d , the dimension of the parametric domain Ω , and $\mathbf{k} = (k_1, k_2, \dots, k_d)$. Here, k_j is the degree of the B-spline basis function $B_{i_j}(\boldsymbol{\eta}_j)$, $j = 1, 2, \dots, d$ (7).

Owing to Lemma 3, the L_2 projector $\mathcal{P} : C(\Omega) \rightarrow \mathbb{S}$, from the continuous function space $C(\Omega)$ to the B-spline sub-space \mathbb{S} , is also bounded in L_∞ norm.

Thus, we have,

Lemma 4. *Denoting $\text{dist}(f, \mathbb{S})$ as the distance from f to the B-spline sub-space \mathbb{S} , we have,*

$$\|\mathcal{D}T - \mathcal{D}T_r\|_\infty = \|f - \mathcal{P}f\|_\infty \leq (1 + \|\mathcal{P}\|_\infty) \text{dist}(f, \mathbb{S}). \quad (13)$$

Proof: For an arbitrary $s \in \mathbb{S}$, it holds that $\mathcal{P}s = s$. Letting \mathcal{I} is the identity operator, we have,

$$\|f - \mathcal{P}f\|_\infty = \|f - s + \mathcal{P}s - \mathcal{P}f\|_\infty = \|(\mathcal{I} - \mathcal{P})(f - s)\|_\infty \leq (1 + \|\mathcal{P}\|_\infty) \|f - s\|_\infty.$$

Because s is an arbitrary function in \mathbb{S} , it can be so chosen that $\|f - s\|_\infty = \text{dist}(f, \mathbb{S})$. Thus, Eq. (13) is proved. \square

Therefore, if $\text{dist}(f, \mathbb{S}) \rightarrow 0$, when $h \rightarrow 0$, we get $\|\mathcal{D}T - \mathcal{D}T_r\|_\infty \rightarrow 0$, when $h \rightarrow 0$. In other words, the IGA-L method is consistency. Here, h is the knot grid size of \mathcal{T}^h , where the splines in \mathbb{S} are defined on. In conclusion, the theorem follows.

Theorem 1. *Suppose the operators \mathcal{D} and \mathcal{G} have polynomial coefficients. If $\text{dist}(f, \mathbb{S}) \rightarrow 0$, when $h \rightarrow 0$, the IGA-L method is consistency.*

3.1.2. Consistency in the generic case

In this section, we consider the case that the operators \mathcal{D} and \mathcal{G} in Eq. (1) are generic operators. Give three knot sequences,

$$\{\underbrace{u_0, u_0, \dots, u_0}_{l_u+1}, u_1, \dots, u_{n_u-1}, \underbrace{u_{n_u}, u_{n_u}, \dots, u_{n_u}}_{l_u+1}\}, \quad (14)$$

$$\{\underbrace{v_0, v_0, \dots, v_0}_{l_v+1}, v_1, \dots, v_{n_v-1}, \underbrace{v_{n_v}, v_{n_v}, \dots, v_{n_v}}_{l_v+1}\}, \quad (15)$$

$$\{\underbrace{w_0, w_0, \dots, w_0}_{l_w+1}, w_1, \dots, w_{n_w-1}, \underbrace{w_{n_w}, w_{n_w}, \dots, w_{n_w}}_{l_w+1}\}. \quad (16)$$

In one dimensional case, the numerical solution T_r is defined on the knot sequence (14); in two dimensional case, T_r is defined on the knot sequences (14) and (15); in three dimensional case, T_r is defined on the knot sequences (14), (15), and (16). Denote h as the knot grid size of the knot grid where T_r is defined on.

Let $R(\boldsymbol{\eta}) = (\mathcal{D}T(\boldsymbol{\eta}) - \mathcal{D}T_r(\boldsymbol{\eta}))^2$, $\boldsymbol{\eta} \in \Omega_0$. Denote $H_u = u_{n_u} - u_0$, $H_v = v_{n_v} - v_0$, $H_w = w_{n_w} - w_0$, and $e_h = \sum_k R(\boldsymbol{\vartheta}_k)$ as the least-squares fitting error, where $\boldsymbol{\vartheta}_k \in \Omega_0$ are collocation points. The following theorem holds.

Theorem 2. *In the IGA-L method, if*

- (1) *each knot interval of the NURBS function T_r defined on knot grid \mathcal{T}^h contains at least one collocation point, and,*
- (2) *the degree of each variable in T_r is larger than the maximum order of the partial derivatives to the variables appearing in \mathcal{D} (see Eq. (1)),*

the fitting error of $\mathcal{D}T_r$ to $\mathcal{D}T$ in L_2 norm can be deduced as,

- (1) *in one dimensional case,*

$$\|\mathcal{D}T - \mathcal{D}T_r\|_2^2 \leq h e_h + h H_u |R'(\boldsymbol{\eta}^*)|, \text{ where } \boldsymbol{\eta}^* \in (u_0, u_{n_u}); \quad (17)$$

- (2) *in two dimensional case,*

$$\|\mathcal{D}T - \mathcal{D}T_r\|_2^2 \leq h^2 e_h + h H_u H_v (|R'_u(\tilde{\boldsymbol{\eta}}_1, \tilde{\xi}_1)| + |R'_v(\tilde{\boldsymbol{\eta}}_2, \tilde{\xi}_2)|), \quad (18)$$

where $(\tilde{\boldsymbol{\eta}}_1, \tilde{\xi}_1), (\tilde{\boldsymbol{\eta}}_2, \tilde{\xi}_2)$ are points in $(u_0, u_{n_u}) \times (v_0, v_{n_v})$;

- (3) *in three dimensional case,*

$$\|\mathcal{D}T - \mathcal{D}T_r\|_2^2 \leq h^3 e_h + h H_u H_v H_w (|R'_u(\tilde{\boldsymbol{\eta}}_1, \tilde{\xi}_1)| + |R'_v(\tilde{\boldsymbol{\eta}}_2, \tilde{\xi}_2)| + |R'_w(\tilde{\boldsymbol{\eta}}_3, \tilde{\xi}_3)|), \quad (19)$$

where $(\tilde{\boldsymbol{\eta}}_1, \tilde{\xi}_1), (\tilde{\boldsymbol{\eta}}_2, \tilde{\xi}_2)$, and $(\tilde{\boldsymbol{\eta}}_3, \tilde{\xi}_3)$ are points in $(u_0, u_{n_u}) \times (v_0, v_{n_v}) \times (w_0, w_{n_w})$.

The proof to the three formulae (17)- (19) in one-, two-, and three-dimensional cases are similar. We present the proof to the two-dimensional case (Eq. (18)) in Appendix A6.

Moreover, if the derivative or partial derivative of $R(\boldsymbol{\eta})$ is continuous, (then it is bounded in its domain), and the least-squares fitting error e_h is also bounded, we have $\|\mathcal{D}T - \mathcal{D}T_r\|_2^2 \rightarrow 0$, ($h \rightarrow 0$), based on Theorem 2. That is, the IGA-L method is consistency. This leads to the following theorem.

Theorem 3. *If the least-square fitting error e_h is bounded, $R(\boldsymbol{\eta}) \in C^1(\Omega_0)$, and the conditions in Theorem 2 are satisfied, then the IGA-L method is consistency.*

3.2. Convergence

Based on the consistency property of IGA-L, we can show that IGA-L is convergent if the differential operator is stable or strongly monotonic, similarly as in Ref. [39].

Let V and W be two Hilbert spaces and $\|\cdot\|_V$ and $\|\cdot\|_W$ be two norms defined on V and W , respectively. Suppose $\|\cdot\|_V$ and $\|\cdot\|_W$ are equivalent to the L^2 norm, i.e., there exist positive constants α_V , β_V , α_W , and β_W such that,

$$\alpha_V \|\cdot\|_{L^2} \leq \|\cdot\|_V \leq \beta_V \|\cdot\|_{L^2}, \quad (20)$$

$$\alpha_W \|\cdot\|_{L^2} \leq \|\cdot\|_W \leq \beta_W \|\cdot\|_{L^2}. \quad (21)$$

We first give the definitions for stable and strongly monotonic operators.

Definition 1 (Stability estimate and stable operator [52]). Let V, W be Hilbert spaces and $\mathcal{D} : V \rightarrow W$ be a differential operator. If there exists a constant $C_S > 0$ such that

$$\|\mathcal{D}v\|_W \geq C_S \|v\|_V, \quad \text{for all } v \in D(\mathcal{D}), \quad (22)$$

where $D(\mathcal{D})$ represents the domain of \mathcal{D} , differential operator \mathcal{D} is called the stable operator, and the inequality (22) is called the stability estimate.

Definition 2 (Strongly monotonic operator [52]). Let V be a Hilbert space and $\mathcal{D} \in \mathcal{L}(V, V')$. Operator \mathcal{D} is said to be a strongly monotonic operator, if there exists a constant $C_D > 0$, such that

$$\langle \mathcal{D}v, v \rangle \geq C_D \|v\|_V^2, \quad \text{for all } v \in V. \quad (23)$$

For every $v \in V$, element $\mathcal{D}v \in V'$ is of a linear form. The symbol $\langle \mathcal{D}v, v \rangle$, which denotes the application of $\mathcal{D}v$ to $v \in V$, is called a duality pairing.

Clearly, if a differential operator \mathcal{D} is strongly monotonic, it is stable.

Lemma 5. Let V be a Hilbert space and $\mathcal{D} \in \mathcal{L}(V, V')$ be a continuous strongly monotonic linear operator. Then, there exists a constant $C_D > 0$ such that \mathcal{D} satisfies the stability estimate (22) [52].

The proof can be found in Ref. [39].

Therefore, we have the convergence property of IGA-L as follows.

Theorem 4. Suppose NURBS function T_r , defined on knot grid \mathcal{T}^h , is the numerical solution to the boundary value problem (1), generated by IGA-L, and the conditions presented in Theorem 3 are satisfied in one, two, and three dimensions, respectively. If differential operator $\mathcal{D} : V \rightarrow W$ in (1) is a stable operator, T_r will converge to analytic solution T when the knot grid size $h \rightarrow 0$.

Proof: Differential operator \mathcal{D} in (1) is a stable operator, so there exists a constant $C_S > 0$, such that

$$\|\mathcal{D}(T - T_r)\|_W \geq C_S \|T - T_r\|_V.$$

And it is equivalent to

$$\|T - T_r\|_V \leq \frac{1}{C_S} \|\mathcal{D}T - \mathcal{D}T_r\|_W.$$

Due to the equivalence of $\|\cdot\|_{L^2}$ and $\|\cdot\|_W$ (20), we have,

$$\|T - T_r\|_V \leq \frac{1}{C_S} \|\mathcal{D}T - \mathcal{D}T_r\|_W \leq \frac{\beta_W}{C_S} \|\mathcal{D}T - \mathcal{D}T_r\|_{L^2}.$$

Because of the consistency of IGA-L (Theorem 3), $\|T - T_r\|_V$ will converge to 0 when $h \rightarrow 0$. And this theorem is proved. \square

Moreover, Theorem 4 and Lemma 5 lead to the direct corollary.

Corollary 1. *Suppose NURBS function T_r defined on knot grid \mathcal{T}^h is the numerical solution to the boundary value problem (1), generated by IGA-L, and the conditions presented in Theorem 3 are satisfied in one, two, and three dimensions, respectively. Additionally, suppose norm $\|\cdot\|_{L^2}$ bounds norm $\|\cdot\|_V$. If differential operator \mathcal{D} in (1) is a strongly monotonic operator, then T_r will converge to analytic solution T when $h \rightarrow 0$.*

It is well known that a wide class of elliptic differential operators are stable or strongly monotonic. Hence, IGA-L is convergent for equations that have these elliptic differential operators. The examples of a PDE whose differential operators are strongly monotonic can be found in Refs. [52, 39].

4. Comparisons and discussions

4.1. Theoretical comparisons

In the following, we compare IGA-L with IGA-C and IGA-SC in terms of their computational efficiency at solving a scalar problem (Laplace equation [38]) and vector problem (elasticity equation [38]). We consider model discretizations in one, two, and three dimensions that are characterized by the degree of the basis functions and the numbers of control and collocation points in each parametric direction. For the sake of simplicity, we assume that the model discretizations in two and three dimensions have the same number of collocation points (and control points) in each parametric direction, and the degrees of basis functions in one, two, and three dimensions are p , $p \times p$, and $p \times p \times p$, respectively.

First, the costs in floating point operations (flops) for the formation at one collocation point are the same for IGA-L, IGA-C, and IGA-SC. These costs are listed in Table 1.

Second, we compared the costs (in flops) of solving the linear system of equations in IGA-C, IGA-SC, and IGA-L, and present the comparison in Table 2. In this table, the first column is the dimension of the problem solved, and the second column is the number of control points (equal to the number of collocation points in IGA-C). The third column is the cost in flops to solve the linear system of equations using Gaussian elimination in IGA-C [49]. Moreover, the fourth column is the number of collocation points in IGA-L, and the fifth column is the cost in flops to solve the normal equation (5) using Cholesky decomposition in IGA-L [49]. Finally, the last two columns are the number of collocation points in IGA-SC, and the cost in flops to solve the normal equation using Cholesky decomposition in IGA-SC [49], respectively. We can see that the cost to solve Eq. (5) in IGA-L linearly increases with the number of collocation points (m , $m \times m$, $m \times m \times m$).

Table 1: Cost in flops for formation at one collocation point in IGA-C, IGA-SC, and IGA-L.

Dimension	A scalar problem (Laplace)	A vector problem (elasticity)
Solve for 1st derivatives		
1	$(p + 1)$	
2	$5(p + 1)^2 + 4$	
3	$12(p + 1)^3 + 16$	
Compute right hand side vectors and solve for 2nd derivatives		
1	$3(p + 1)$	
2	$24(p + 1)^2 + 16$	
3	$87(p + 1)^3 + 140$	
Total number of flops for basis function		
1	$35(p + 1) + 1$	
2	$124(p + 1)^2 + 33$	
3	$302(p + 1)^3 + 219$	
Evaluate Navier's eqs. on global level		
1	$(p + 1)$	
2	$12(p + 1)^2$	
3	$21(p + 1)^3$	
Total number of flops to evaluate the local stiffness matrix		
1	$35(p + 1) + 1$	$36(p + 1) + 1$
2	$125(p + 1)^2 + 33$	$134(p + 1)^2 + 33$
3	$304(p + 1)^3 + 219$	$323(p + 1)^3 + 219$

Table 2: Cost comparison of IGA-C, IGA-SC, and IGA-L.

Dim. ¹	#Cont. ²	IGA-C	IGA-L		IGA-SC	
		Cost ³	#Col. ⁴	Cost ³	#Col. ⁴	Cost ³
$d = 1$	n	$2n^3/3$	m	$n^3/3 + mn^2$	$2(n - p)$ (odd p)	$n^3/3 + (2n - p)n^2$
					$2(n - p) - 1$ (even p)	$n^3/3 + (2(n - p) - 1)n^2$
$d = 2$	n^2	$2n^6/3$	m^2	$n^6/3 + m^2n^4$	$(2(n - p))^2$ (odd p)	$n^6/3 + (2(n - p))^2n^4$
					$(2(n - p) - 1)^2$ (even p)	$n^6/3 + (2(n - p) - 1)^2n^4$
$d = 3$	n^3	$2n^9/3$	m^3	$n^9/3 + m^3n^6$	$(2(n - p))^3$ (odd p)	$n^9/3 + (2(n - p))^3n^6$
					$(2(n - p) - 1)^3$ (even p)	$n^9/3 + (2(n - p) - 1)^3n^6$

¹ Dimension.

² Number of control points.

³ Cost in flops.

⁴ Number of collocation points.

4.2. Numerical comparisons

In this section, we compare IGA-L with IGA-C and IGA-SC using some numerical examples. To measure the approximation accuracy, we define the error formulae, i.e., the *relative error for*

the solution T_r ,

$$e_T = \sqrt{\frac{\int_{\Omega} (T - T_r)'(T - T_r) d\Omega}{\int_{\Omega} T' T d\Omega}}. \quad (24)$$

Additionally, to illustrate the error distribution of the numerical solution, the following *absolute errors* e_a are employed, i.e.,

$$\begin{aligned} e_a(u) &= |T(u) - T_r(u)|, \text{ for one-dimensional case,} \\ e_a(u, v) &= |T(u, v) - T_r(u, v)|, \text{ for two-dimensional case,} \\ e_a(u, v, w) &= |T(u, v, w) - T_r(u, v, w)|, \text{ for three-dimensional case.} \end{aligned} \quad (25)$$

In the following, six numerical examples are presented. These examples are implemented with MATLAB and run on a PC with a 2.66-GHz Intel Core2 Quad CPU Q9400 and 3 GB memory. Examples I–III are three source problems in one, two, and three dimensions, respectively, Example IV is a linear elasticity problem, and Example V demonstrates the stability of the IGA-L method with respect to that of the IGA-C method. Moreover, Example VI illustrates the capability of IGA-L method for solving a 2D source problem on a frame-corner-like domain which contains a C^0 line. The problems in Examples I–V are solved by IGA-L, IGA-C, and IGA-SC methods. With the IGA-C method, the control points are increased gradually, and the collocation points are the Greville abscissae [2] of the knot vectors, also called the *Greville collocation points*. The collocation manner for IGA-SC follows the method developed in [40]. With the IGA-L method, the control points are variable and are increased gradually at the same rate as those of IGA-C. In each computation round of the IGA-L variable strategy, supposing the numbers of the control points are n , $n \times n$, and $n \times n \times n$ in the one-, two-, and three-dimensional cases, respectively, the numbers of the corresponding collocation points are taken as $n + 2$, $(n + 2) \times (n + 2)$, and $(n + 2) \times (n + 2) \times (n + 2)$, respectively. In this paper, we take the following collocation manner for IGA-L method.

Collocation manner for IGA-L: The collocation points for IGA-L are taken as the Greville abscissae of a knot sequence. To produce n Greville collocation points for a NURBS curve of degree k , ($n \geq k$), we first uniformly insert $n - k - 1$ numbers into the interval $[0, 1]$, resulting in the knot sequence,

$$\underbrace{0, 0, \dots, 0}_k, \frac{1}{n-k}, \frac{2}{n-k}, \dots, \frac{n-k-1}{n-k}, \underbrace{1, 1, \dots, 1}_k,$$

and then, n Greville collocation points for a NURBS curve of degree k , ($n \geq k$) can be generated from the above knot sequence. The collocation points for NURBS surfaces and solids can be produced by the aforementioned manner for each parameter.

Example I: one-dimensional source problem with Dirichlet boundary condition:

$$\begin{cases} -T'' + T = (1 + 4\pi^2) \sin(2\pi x), & x \in \Omega = [0, 1], \\ T(0) = 0, T(1) = 0. \end{cases} \quad (26)$$

This problem's analytical solution is $T = \sin(2\pi x)$. The physical domain $\Omega = [0, 1]$ of the boundary problem (26) is represented by a cubic B-spline curve. For the mathematical representation of the cubic B-spline curve, please refer to Appendix A1.

The analytical, IGA-L, IGA-SC and IGA-C solutions for the one-dimensional source problem (26) with cubic B-spline, are illustrated in Fig. 1(a), where the IGA-L solution was generated

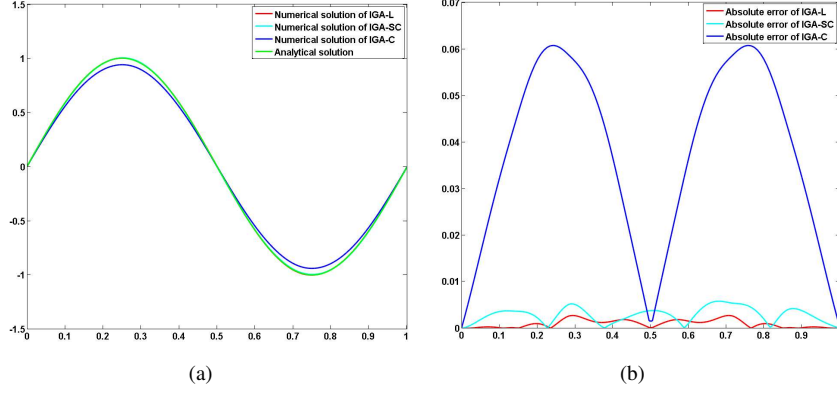


Figure 1: Comparison of the analytical, IGA-L, IGA-SC and IGA-C solutions of Eq. (26). (a) Analytical solution, IGA-L, IGA-SC and IGA-C solutions. Note that the analytical solution almost overlaps the IGA-L and IGA-SC solutions. (b) Absolute error distribution curves of the IGA-L, IGA-SC and IGA-C solutions.

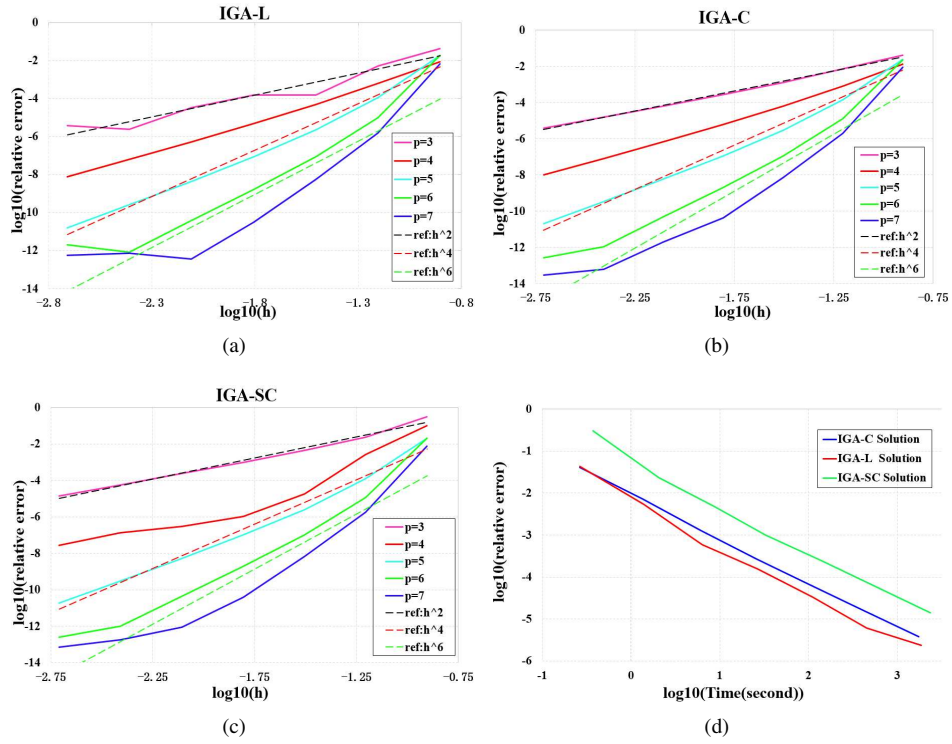


Figure 2: Numerical results for the 1D source problem (26). Diagrams of $\log_{10}(h)$ v.s. $\log_{10}(\text{relative error})$ for IGA-L (a), IGA-C (b), and IGA-SC (c), respectively. And, diagram of $\log_{10}(\text{Time})$ v.s. $\log_{10}(\text{relative error})$ (d).

with 10 control points and 14 Greville collocation points, IGA-SC solution was generated with

10 control point and 14 collocation points, and IGA-C solution was generated with 10 control points. The relative errors for the IGA-L, IGA-SC, and IGA-C solutions are 0.0018, 0.0023, and 0.0598. The relative error for the IGA-L solution is one order of magnitude less than that of the IGA-C solution. In addition, Fig. 1(b) demonstrates the absolute error distribution curves of the IGA-L, IGA-SC, and IGA-C solutions, respectively. The maximum absolute errors of IGA-L, IGA-SC, and IGA-C solutions are 0.0028, 0.0034, and 0.0607, respectively.

Moreover, diagrams of $\log_{10}(h)$ v.s. $\log_{10}(\text{relative error})$ for IGA-L, IGA-C, and IGA-SC, are illustrated in Figs. 2(a)- 2(c), respectively. From these diagrams, it can be seen that, in solving the one-dimensional source problem (26), the convergence rates of IGA-L, IGA-C, and IGA-SC are all $O(h^p)$ for even p , and $O(h^{p-1})$ for odd p . Additionally, the diagrams of $\log_{10}(\text{time})$ v.s. $\log_{10}(\text{relative error})$ for IGA-L, IGA-SC, and IGA-C methods are demonstrated in Fig. 2(d), and the performance of the IGA-L method is the best.

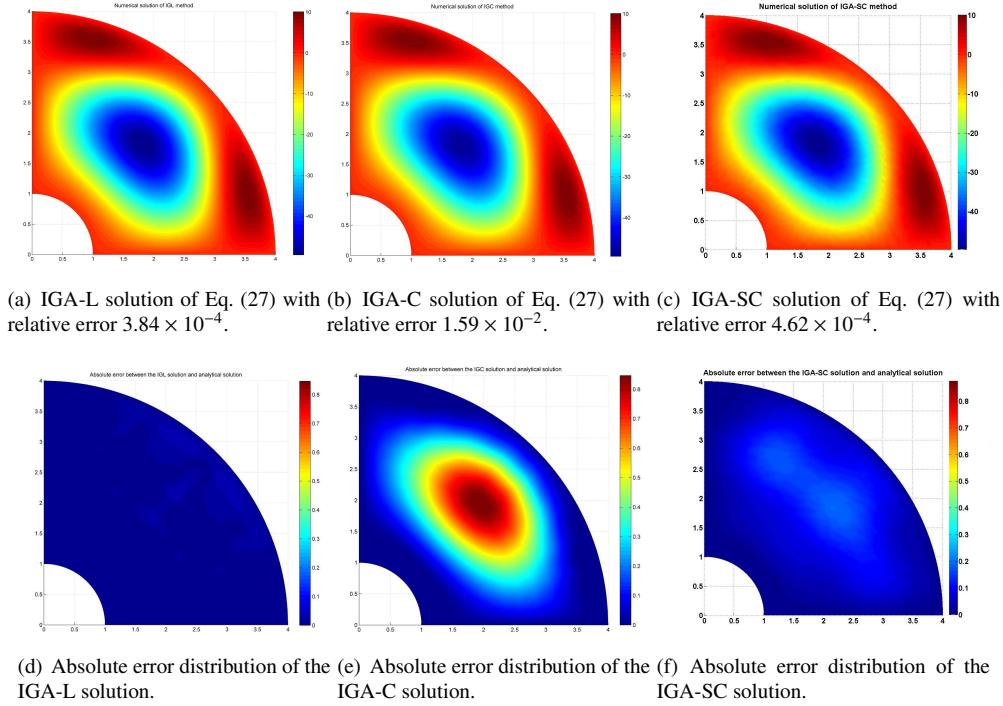


Figure 3: Comparison of the analytical, IGA-L, IGA-C, and IGA-SC solutions of Eq. (27). The relative error of the IGA-L solution is nearly two orders of magnitude less than the IGA-C solution.

Example II: source problem in the two-dimensional domain Ω ,

$$\begin{cases} -\Delta T + T = f, & (x, y) \in \Omega \\ T|_{\partial\Omega} = 0, \end{cases} \quad (27)$$

where Ω is a quarter of an annulus, which can be exactly represented by a cubic NURBS patch

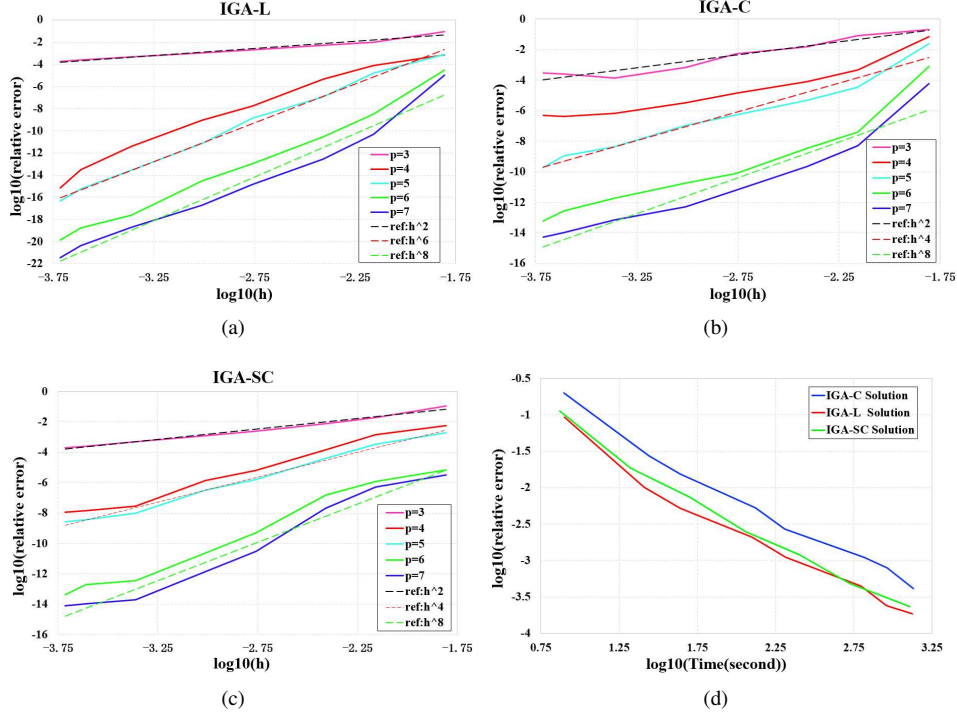


Figure 4: Numerical results for the 2D source problem (27). Diagrams of $\log_{10}(h)$ v.s. $\log_{10}(\text{relative error})$ for IGA-L (a), IGA-C (b), and IGA-SC (c), respectively. And, diagram of $\log_{10}(\text{Time})$ v.s. $\log_{10}(\text{relative error})$ (d).

with 4×4 control points, as presented in Appendix A2, and where

$$\begin{aligned}
 f = & (3x^4 - 67x^2 - 67y^2 + 3y^4 + 6x^2y^2 + 116) \sin(x) \sin(y) \\
 & + (68x - 8x^3 - 8xy^2) \cos(x) \sin(y) \\
 & + (68y - 8y^3 - 8yx^2) \cos(y) \sin(x).
 \end{aligned}$$

The analytical solution of the source problem (27) is

$$T = (x^2 + y^2 - 1)(x^2 + y^2 - 16) \sin(x) \sin(y).$$

Fig. 3 presents numerical solutions of the two-dimensional source problem (27), as generated by the IGA-L, IGA-C and IGA-SC methods. To produce the numerical solutions, we uniformly inserted 11 knots along the u - and v - directions, respectively, to the cubic NURBS patch presented in Appendix A2, resulting in a cubic NURBS patch with 15×15 control points. With 20×20 Greville collocation points, the IGA-L method was employed to solve Eq. (27). The relative error of the IGA-L solution (see Fig. 3(a)) is 3.84×10^{-4} , and Fig. 3(d) illustrates the absolute error distribution of the IGA-L solution. Moreover, the source problem (27) was also solved by the IGA-C method using the same NURBS patch of 15×15 control points (see Fig. 3(b)) with Greville collocation points. The relative error of the IGA-C solution is 1.59×10^{-2} , and its absolute error distribution is illustrated in Fig. 3(e). In this example, the relative error of the IGA-L

solution is two orders of magnitude less than that of the IGA-C solution. In addition, we employed the IGA-SC method to solve the two-dimensional source problem (27), with the same bi-cubic NURBS patch of 15×15 control points (see Fig. 3(b)), and 24×24 collocation points. Note that, even the number of collocation points (24×24) for the IGA-SC method is larger than that for the IGA-L method (20×20), the relative error of the IGA-L solution (3.84×10^{-4}) is still less than that of the IGA-SC solution (4.62×10^{-4}). Fig. 3(f) demonstrates the absolute error distribution of the IGA-SC solution.

Diagrams of $\log_{10}(h)$ v.s. $\log_{10}(\text{relative error})$ for IGA-L, IGA-C, and IGA-SC methods are illustrated in Figs. 4(a)- 4(c), respectively. It should be pointed out that, while the convergence rate of the IGA-SC and IGA-C methods with degree $p = 4, 5$ is $O(h^4)$, that of the IGA-L method with degree $p = 4, 5$ reaches $O(h^6)$. Moreover, Fig. 4(d) presents the diagrams of $\log_{10}(\text{time})$ v.s. $\log_{10}(\text{relative error})$ for the three methods. In these diagrams, the performance of the IGA-L and IGA-SC methods are comparable, both better than that of the IGA-C method.

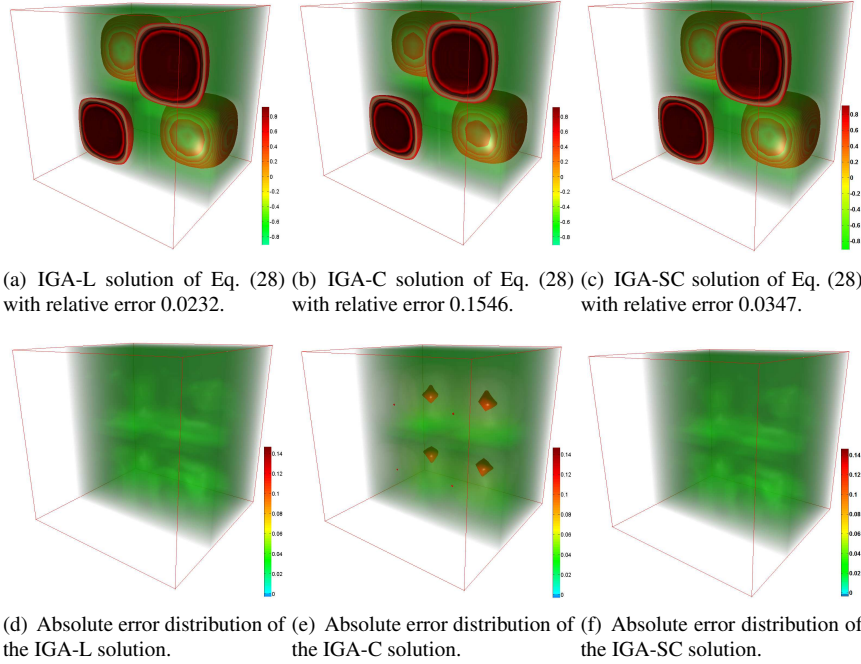


Figure 5: Comparison of the IGA-L, IGA-C and IGA-SC solutions of Eq. (28). The relative error of the IGA-L solution is nearly one order of magnitude less than that of the IGA-C solution.

Example III: source problem defined on the three-dimensional cubic domain $\Omega = [0, 1] \times [0, 1] \times [0, 1]$, i.e.,

$$\begin{cases} -\Delta T + T = f, & (x, y, z) \in \Omega, \\ T|_{\partial\Omega} = 0, \end{cases} \quad (28)$$

where

$$f = (1 + 12\pi^2) \sin(2\pi x) \sin(2\pi y) \sin(2\pi z).$$

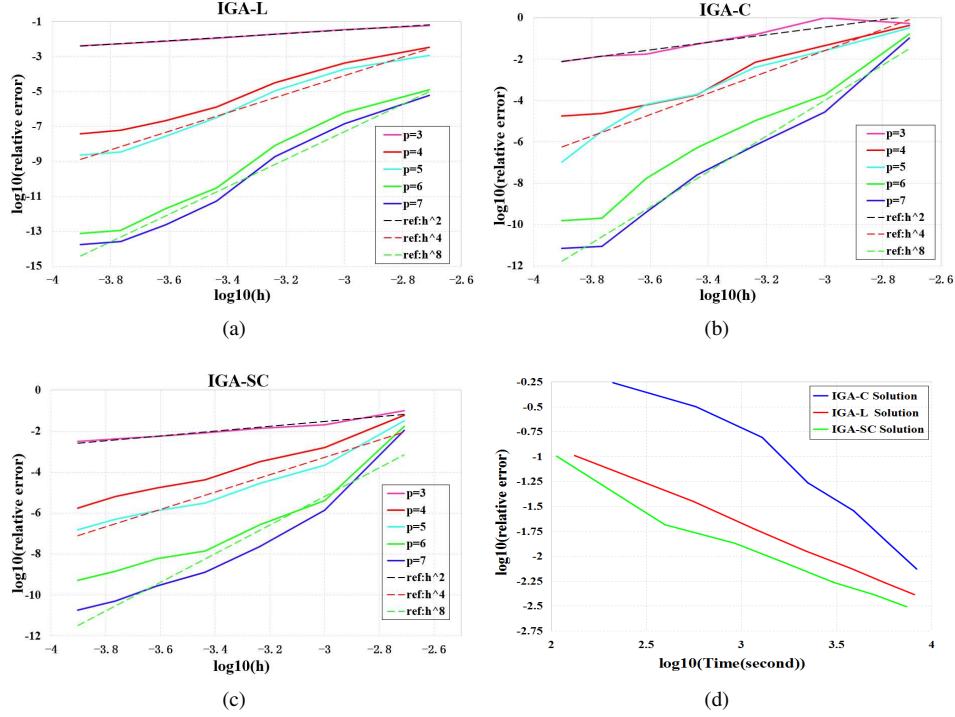


Figure 6: Numerical results for the 3D source problem (28). Diagrams of $\log_{10}(h)$ v.s. $\log_{10}(\text{relative error})$ for IGA-L (a), IGA-C (b), and IGA-SC (c), respectively. And, diagram of $\log_{10}(\text{Time})$ v.s. $\log_{10}(\text{relative error})$ (d).

Its analytical solution is,

$$T = \sin(2\pi x) \sin(2\pi y) \sin(2\pi z).$$

The three-dimensional physical domain Ω is modeled as a cubic B-spline solid with $4 \times 4 \times 4$ control points, as listed in Appendix A3.

In Fig. 5, the IGA-L, IGA-C, and IGA-SC solutions for Eq. (28) are illustrated, where the solutions were generated with tri-cubic B-spline solid. Specifically, to get the IGA-L solution, $7 \times 7 \times 7$ control points and $10 \times 10 \times 10$ Greville collocation points were employed, and the relative error is 0.0232 (see Fig. 5(a)). On the other hand, the relative error for the IGA-C solution with $7 \times 7 \times 7$ control points and Greville collocation points is 0.1456 (Fig. 5(b)). In this example, the relative error of the IGA-L solution is one order of magnitude smaller than that of the IGA-C solution. Moreover, in Fig. 5(c), $10 \times 10 \times 10$ control points and $14 \times 14 \times 14$ collocation points were used to generate the IGA-SC solution with relative error 0.0347. Similar as the two-dimensional case, the relative error of the IGA-SC solution is larger than that of the IGA-L solution, though the numbers of control points and collocation points of IGA-L method are both less than those of the IGA-SC method. Additionally, Figs. 5(d)- 5(f) present the absolute error distribution for the IGA-L, IGA-C, and IGA-SC solutions, respectively.

Furthermore, diagrams of the numerical results for Eq. (28) are illustrated in Fig. 6. Specifically, diagrams of $\log_{10}(h)$ v.s. $\log_{10}(\text{relative error})$ for IGA-L, IGA-C, and IGA-SC are illustrated in Figs 6(a)- 6(c), respectively. From these diagrams, it can be seen that, the convergence

rates of the three methods are all $O(h^2)$ for $p = 3$, $O(h^4)$ for $p = 4, 5$, and $O(h^8)$ for $p = 6, 7$. The diagrams of $\log_{10}(\text{Time})$ v.s. $\log_{10}(\text{relative error})$ for the the three methods are presented in Fig. 6(d), where the performance of IGA-SC method is the best.

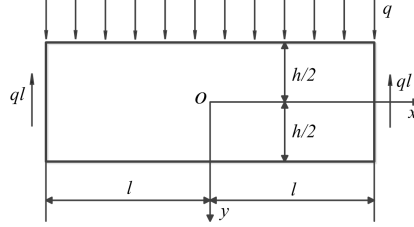


Figure 7: The simply supported beam.

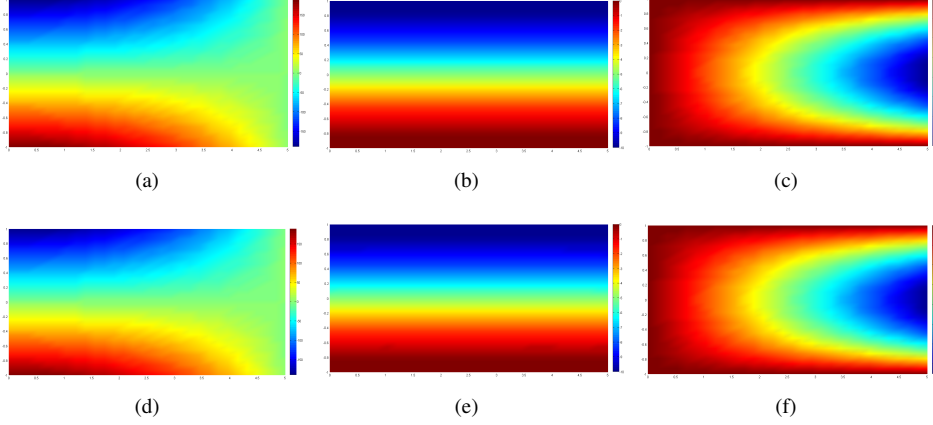


Figure 8: Analytical solution for σ_x (a), σ_y (b), and τ_{xy} (c) and numerical solution for σ_x (d), σ_y (e), and τ_{xy} (f) generated by the IGA-L method with 11×11 control points and 16×16 Greville collocation points.

Example IV: elastic problem, i.e., the simply supported beam (see Fig. 7). As illustrated in Fig. 7, the simply supported beam with a rectangular cross section has depth h and length $2l$. Uniformly distributed loading q was applied on the upper surface, and equilibrium was maintained by reaction force ql at both ends. Here, the body force need not be considered. The analytical solution of the simply supported beam problem is

$$\begin{aligned}\sigma_x &= \frac{6q}{h^3}(l^2 - x^2)y + q\frac{y}{h}\left(4\frac{y^2}{h^2} - \frac{3}{5}\right), \\ \sigma_y &= -\frac{q}{2}\left(1 + \frac{y}{h}\right)\left(1 - \frac{2y}{h}\right)^2, \\ \tau_{xy} &= -\frac{6q}{h^3}x\left(\frac{h^2}{4} - y^2\right).\end{aligned}$$

We calculated the simply supported beam problem using the IGA-L, IGA-C, and IGA-SC methods, with $q = 10$, $h = 2$, $l = 5$ (see Fig. 7). The physical domain was represented by a

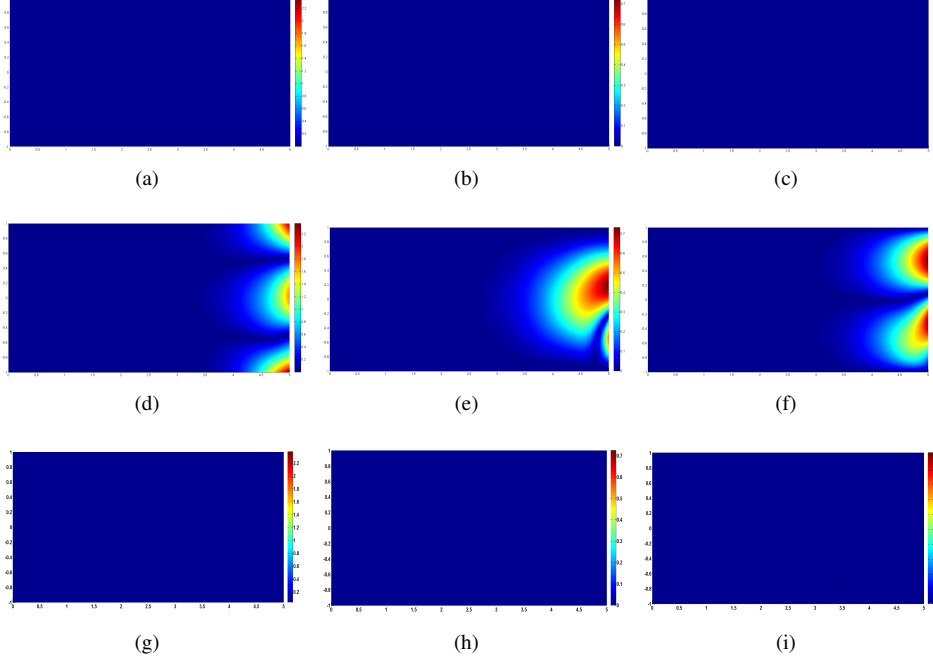


Figure 9: Absolute error (25) distribution for the IGA-L solution σ_x (a), σ_y (b), and τ_{xy} (c), the IGA-C solution σ_x (d), σ_y (e), and τ_{xy} (f), and the IGA-SC solution σ_x (g), σ_y (h), and τ_{xy} (i).

cubic B-spline patch presented in Appendix A4. Fig. 8 illustrates the analytical and numerical solutions for σ_x , σ_y , and τ_{xy} , generated by the IGA-L method with 11×11 control points and 16×16 Greville collocation points. The relative errors for σ_x , σ_y , and τ_{xy} of the IGA-L solutions are 1.10×10^{-5} , 3.29×10^{-4} , and 7.20×10^{-5} , respectively. For comparison, the relative errors for σ_x , σ_y , and τ_{xy} of the IGA-SC solutions with 11×11 control points and 16×16 collocation points are, 3.20×10^{-5} , 4.76×10^{-4} , and 8.70×10^{-5} , respectively; those of the IGA-C solutions with 11×11 control points and Greville collocation points are 4.0×10^{-3} , 6.14×10^{-2} , and 2.15×10^{-2} . Additionally, Fig. 9 demonstrates the absolute error distribution for the IGA-L, IGA-C, and IGA-SC solutions.

Furthermore, in Fig. 10, we demonstrate the diagrams of $\log_{10}(h)$ v.s. $\log_{10}(\text{relative error})$. We can see that, on one hand, while the convergence rate of IGA-C and IGA-SC solutions is $O(h^4)$ for degree $p = 4, 5$, that of IGA-L solutions is $O(h^6)$ for degree $p = 4, 5$. On the other hand, while the convergence rate of IGA-C solutions is $O(h^6)$ for degree $p = 6, 7$, that of IGA-L solutions is $O(h^8)$ for degree $p = 6, 7$. In addition, diagrams of $\log_{10}(\text{time})$ v.s. $\log_{10}(\text{relative error})$ for the three methods IGA-L, IGA-C, and IGA-SC are presented in Fig. 11, and diagrams for IGA-L have the best performance.

Example V (Stability): Note that, in the IGA-C method the number of collocation points is fixed to be equal to the number of control points. However, in the IGA-L method, the number of collocation points is variable and larger than the number of control points. Therefore, the IGA-L method is more flexible than the IGA-C method. In this example, IGA-L, IGA-SC, and IGA-C

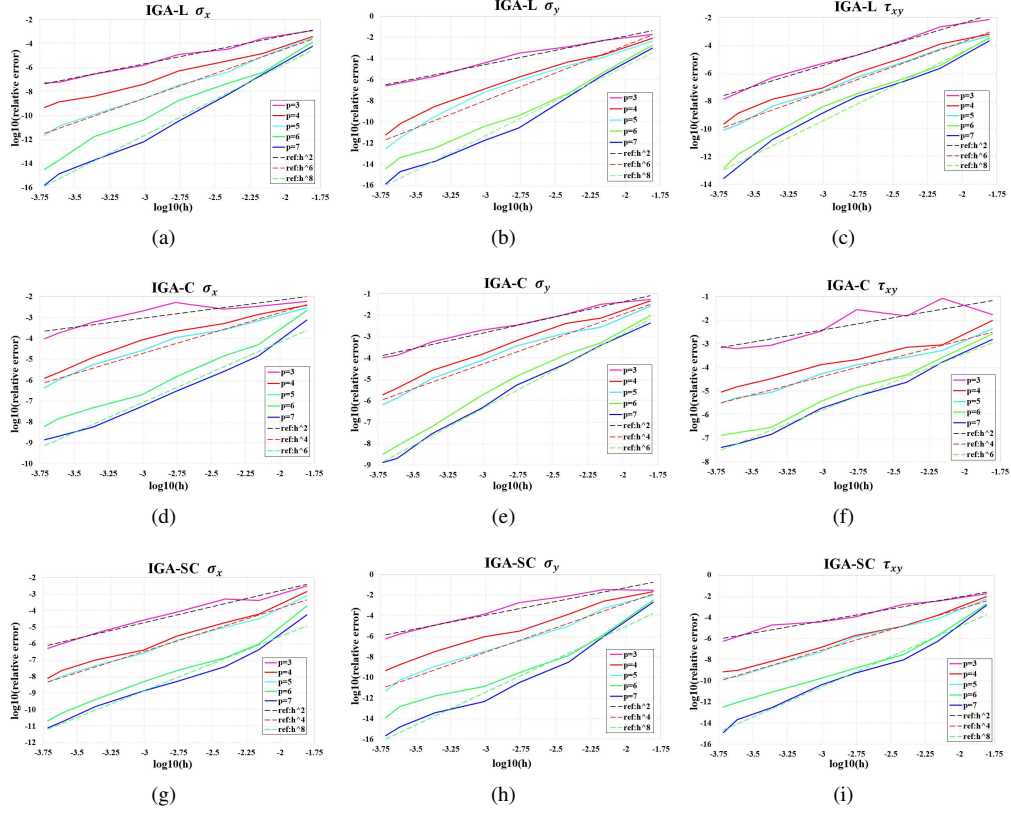


Figure 10: Numerical results for the simply supported beam (Fig. 7). (a, b, c) Diagrams of $\log_{10}(\text{Relative error})$ vs. $\log_{10}(h)$ for σ_x , σ_y , and τ_{xy} , respectively, using IGA-L method. (d, e, f) Diagrams of $\log_{10}(\text{Relative error})$ vs. $\log_{10}(h)$ for σ_x , σ_y , and τ_{xy} , respectively, using IGA-C method. (h, i, j) Diagrams of $\log_{10}(\text{Relative error})$ vs. $\log_{10}(h)$ for σ_x , σ_y , and τ_{xy} , respectively, using IGA-SC method.

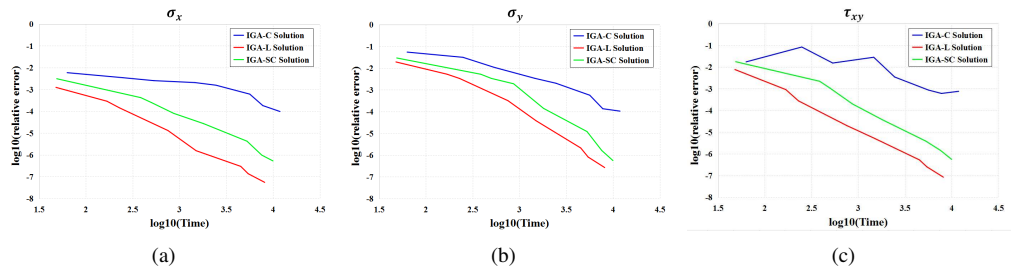
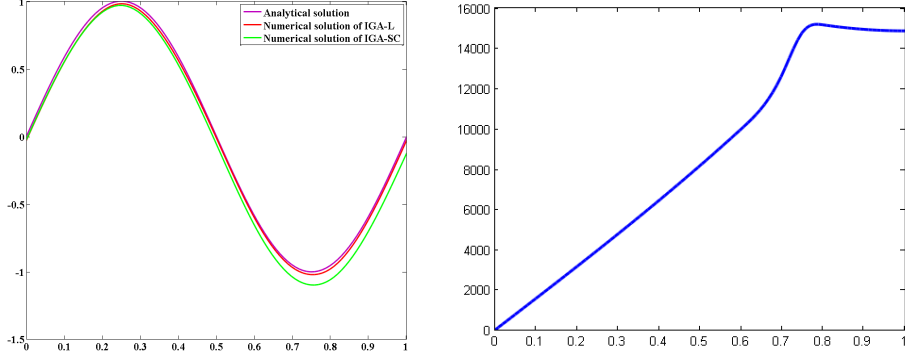


Figure 11: Diagrams of $\log_{10}(\text{Time})$ v.s. $\log_{10}(\text{relative error})$ for the simply supported beam (Fig. 7), for computing δ_x (a), δ_y (b), and τ_{xy} (c), respectively.

are employed to solve a 1D source problem with Dirichlet boundary condition at the left end and



(a) Analytical solution, IGA-L solution with 14 Greville collocation points, and IGA-SC solution with 14 collocation points, of Eq. (29).

(b) Absolute error curve (25) for the IGA-C solution of Eq. (29) with Greville collocation points

Figure 12: IGA-L can be made more stable than IGA-C by changing the number of collocation points when solving Eq. (29). (a) The IGA-L solution to Eq. (29) with 10 control points and 14 Greville collocation points is stable, with relative error 0.0343. Meanwhile, the relative error of the IGA-SC solution to Eq. (29) with 10 control points and 14 Greville collocation points is 0.0567. (b) The IGA-C solution to Eq. (29) with 10 control points and Greville collocation points is unstable, with relative error 2.6245×10^3 .

Neumann boundary condition at the right end, i.e.,

$$\begin{cases} -T'' + T = (1 + 4\pi^2) \sin(2\pi x), & x \in \Omega = [0, 1], \\ T(0) = 0, \\ T'(1) = 2\pi. \end{cases} \quad (29)$$

While the IGA-C method is unstable, the IGA-L method can be made stable by choosing appropriate number of collocation points. The analytical solution of Eq. (29) is $T = \sin(2\pi x)$. We still use the cubic B-spline curve, presented in Appendix A1, to represent the physical domain $\Omega = [0, 1]$.

Consider the case where the analytic solution of Eq. (29) is approximated by a cubic B-spline function with 10 control points, generated by inserting the following knots

$$0.25, 0.5, 0.6, 0.7, 0.75, 0.8,$$

into the cubic B-spline curve in Appendix A1. When we use IGA-C to solve the source problem (29) with Greville collocation points, the numerical solution is unstable, with relative error (24) 2.6245×10^3 (Fig. 12(b)). However, when IGA-L is employed to solve the source problem (29) with 14 Greville collocation points, the solution is stable, with relative error 0.0343 (Fig. 12(a)). In addition, though the IGA-SC solution with 14 Greville collocation points to Eq.(29) is also stable, its relative error is 0.0567, larger than that of the IGA-L solution.

Example VI (Frame Corner): In this example, we solve a 2D source problem defined on the domain of frame corner (Fig. 13(a)), i.e.,

$$\begin{cases} -\Delta T + T = f, & (x, y) \in \Omega \\ T|_{\partial\Omega} = 0, \end{cases} \quad (30)$$

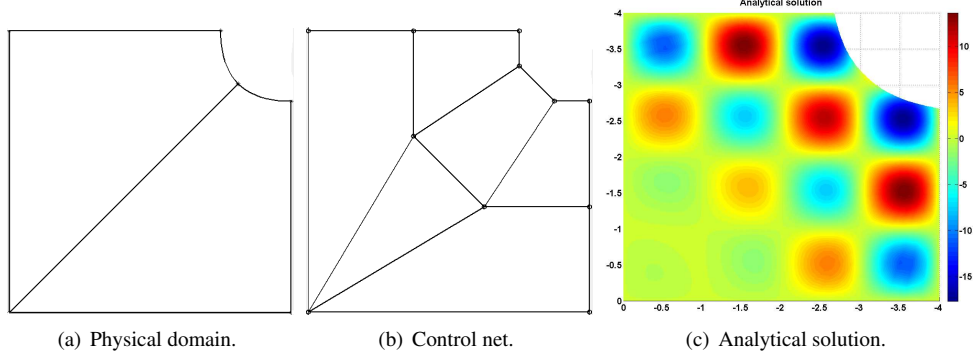


Figure 13: Physical domain (a), control net (b), and the analytical solution (c) on the domain of frame corner.

where

$$f = (-4 + (2\pi^2 + 1)x^2 + (2\pi^2 + 1)y^2 - (2\pi^2 + 1)) \sin(\pi x) \sin(\pi y) - 4\pi x \cos(\pi x) \sin(\pi y) - 4\pi y \cos(\pi y) \sin(\pi x).$$

The analytical solution of the 2D source problem (Eq. (30)) is (Fig 13(c)),

$$T = (x^2 + y^2 - 1) \sin(\pi x) \sin(\pi y).$$

The physical domain of the 2D source problem (30) is a frame-corner-like shape (see Fig. 13(a)), which is modeled by a bi-quadratic NURBS surface with two patches (see Appendix A5). Fig. 13(b) illustrates the control net of the bi-quadratic NURBS surface, where there are two overlapping control points at the lower left corner. So, the two patches are C^0 continuous across their common boundary inside the domain (Fig. 13(a)). In other words, the physical domain contains a C^0 line (Fig. 13(a)).

In this example, we compare the IGA-L method with IGA-C, IGA-SC, and isogeometric Galerkin method (IGA-G). Fig. 14 illustrates the numerical solutions generated by IGA-L, IGA-G, IGA-C, and IGA-SC methods. All of the numerical solutions are bi-cubic NURBS functions with 17×18 control points. The relative error of IGA-C solution is 5.42×10^{-2} (Fig.14(c)). Using 64×65 quadrature points, the relative error of IGA-G solution is 4.25×10^{-4} (Fig.14(b)). With 28×30 collocation points, the relative error of IGA-SC method is 8.53×10^{-4} . However, the relative error of our IGA-L method reaches 7.84×10^{-4} using 24×26 collocation points. Note that, the number of collocation points of our IGA-L method is smaller than that of IGA-SC method, but the precision of IGA-L method is better than that of IGA-SC method.

Moreover, Fig. 15 demonstrates the absolute error distributions of IGA-L, IGA-G, IGA-C, and IGA-SC solutions. It can be noticed that, while the absolute error distribution of IGA-C method is heavily influenced by the C^0 line of the the physical domain (Fig. 15(c)), the C^0 line almost does not affect the absolute error distribution of IGA-L method (Fig. 15(a)). Moreover, compared with the IGA-SC method (Fig. 15(d)), the absolute error distribution of IGA-L method (Fig. 15(a)) is closer to that of IGA-G method (Fig. 15(b)).

Finally, in Fig. 16, we present diagrams of $\log_{10}(h)$ v.s. $\log_{10}(\text{relative error})$, and diagram of $\log_{10}(\text{time})$ v.s. $\log_{10}(\text{relative error})$ for IGA-L, IGA-G, IGA-C, and IGA-SC methods. From diagrams of $\log_{10}(h)$ v.s. $\log_{10}(\text{relative error})$ (Figs.16(a)-16(d)), we can see that the convergence rates of IGA-L, IGA-G, and IGA-SC are the same, i.e., $O(h^2)$ for degree $p = 3$, $O(h^6)$ for degrees

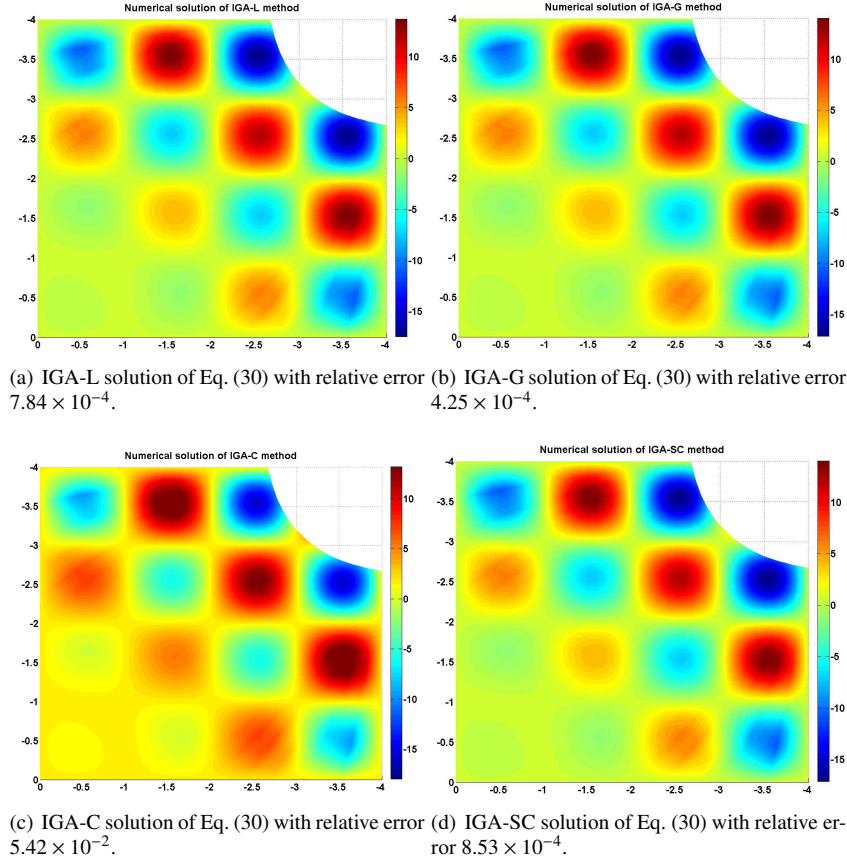


Figure 14: The numerical solutions by IGA-L (a), IGA-G (b), IGA-C (c), and IGA-SC (d) methods, respectively.

$p = 4$ and 5 , $O(h^8)$ for degree $p = 6$ and 7 . Lastly, from diagram of $\log_{10}(\text{time})$ v.s. $\log_{10}(\text{relative error})$, IGA-L method is better than IGA-SC and IGA-C methods.

5. Conclusion

IGA approximates the solution of a boundary value problem (or initial value problem) by a NURBS function. In this paper, we developed the IGA-L method to determine the unknown coefficients of the approximate NURBS function by fitting the sampling values in the least-squares sense. We proved the consistency and convergence properties of IGA-L. Moreover, the many numerical examples presented in this paper show that a small computational increase in IGA-L leads to large improvements in the accuracy, and furthermore that IGA-L is more flexible and more stable than IGA-C.

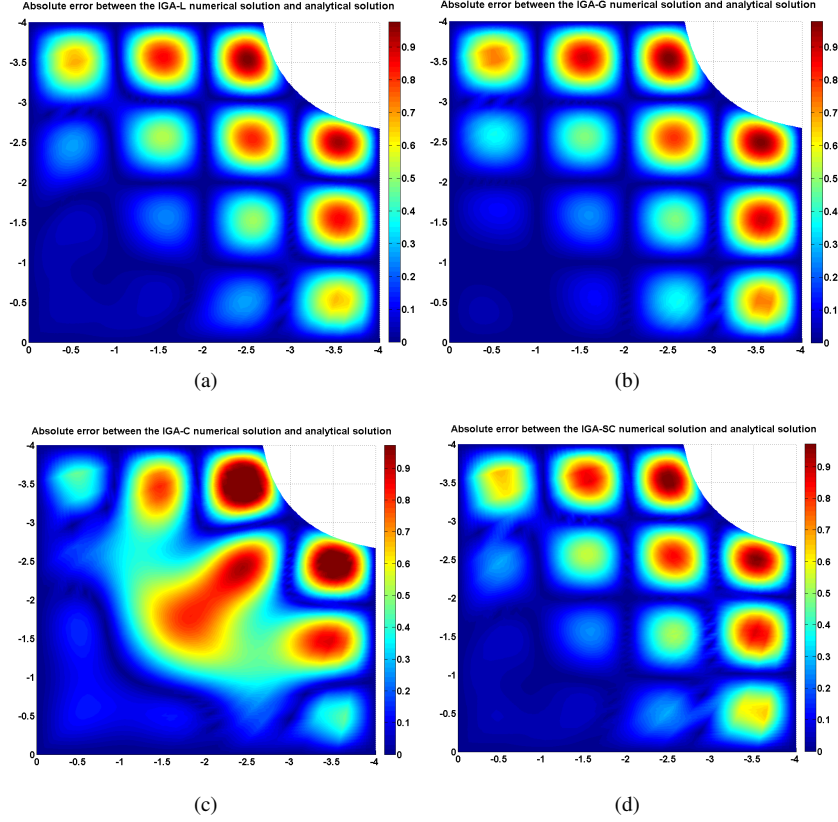


Figure 15: Absolute error distributions for IGA-L solution (a), IGA-G solution (b), IGA-C solution (c), and IGA-SC solution (d), respectively.

Acknowledgement

This work is supported by the National Natural Science Foundation of China (Grant Nos. 61379072, 61202201, 60970150). Dr. Qianqian Hu is also supported by the Open Project Program (No. A1305) of the State Key Lab of CAD&CG, Zhejiang University.

Appendix

In Appendix A1-A5, we list the control points, knot vector, and weights of the NURBS representation of the physical domains in the numerical examples. In Appendix A6, the proof to the formula (18) in the two dimensional case in Theorem 2 is presented.

A1: NURBS representation of the physical domain in Examples I and IV

The physical domain in Examples I and IV is represented by a cubic B-spline curve. Its control points are listed in the following Table 3.

The knot vector is

$$0 \ 0 \ 0 \ 1 \ 1 \ 1 \ 1.$$

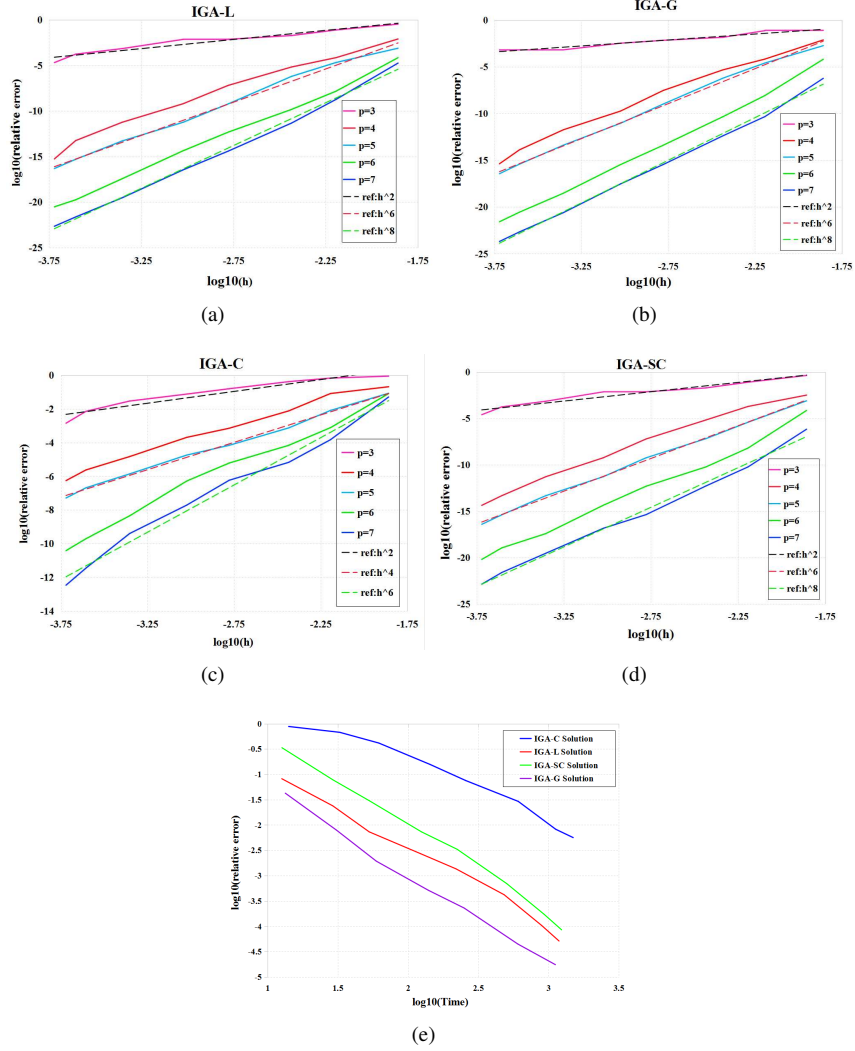


Figure 16: Diagrams of $\log_{10}(h)$ v.s. $\log_{10}(\text{relative error})$ for IGA-L (a), IGA-G (b), IGA-C (c), and IGA-SC (d) methods, respectively. And, diagram of $\log_{10}(\text{time})$ v.s. $\log_{10}(\text{relative error})$ for the four methods (e).

Table 3: Control points of the cubic B-spline curve in Examples I and IV

B_1	B_2	B_3	B_4
0	$\frac{1}{3}$	$\frac{2}{3}$	1

A2: NURBS representation of the physical domain in Example II

The physical domain in Example II is represented by a cubic NURBS patch. Its control points are listed in Table 4, and Table 5 presents its weights. The knot vectors along u - and v -direction

are, respectively,

$$\begin{aligned} &00001111, \\ &00001111. \end{aligned}$$

Table 4: Control points of the quarter of annulus

i	$B_{i,1}$	$B_{i,2}$	$B_{i,3}$	$B_{i,4}$
1	(1,0)	(2,0)	(3,0)	(4,0)
2	$(1, 2-\sqrt{2})$	$(2, 4-2\sqrt{2})$	$(3, 6-3\sqrt{2})$	$(4, 8-4\sqrt{2})$
3	$(2-\sqrt{2}, 1)$	$(4-2\sqrt{2}, 2)$	$(6-3\sqrt{2}, 3)$	$(8-4\sqrt{2}, 4)$
4	(0,1)	(0,2)	(0,3)	(0,4)

Table 5: Weights for the quarter of annulus

i	$\omega_{i,1}$	$\omega_{i,2}$	$\omega_{i,3}$	$\omega_{i,4}$
1	1	1	1	1
2	$\frac{1+\sqrt{2}}{3}$	$\frac{1+\sqrt{2}}{3}$	$\frac{1+\sqrt{2}}{3}$	$\frac{1+\sqrt{2}}{3}$
3	$\frac{1+\sqrt{2}}{3}$	$\frac{1+\sqrt{2}}{3}$	$\frac{1+\sqrt{2}}{3}$	$\frac{1+\sqrt{2}}{3}$
4	1	1	1	1

A3: NURBS representation of the physical domain in Example III

The physical domain in Example III is represented by a cubic B-spline solid. Its control points are listed in Table 6. The knot vectors along u -, v -, and w -directions are, respectively,

$$\begin{aligned} &00001111, \\ &00001111, \\ &00001111. \end{aligned}$$

A4: NURBS representation of the physical domain in Example IV

The physical domain in Example IV is represented by a cubic B-spline patch. Its control points are listed in Table 7. The knot vectors along u -, and v -directions are, respectively,

$$\begin{aligned} &00001111, \\ &00001111. \end{aligned}$$

A5: NURBS representation of the physical domain in Example VI

The physical domain of frame corner in Example VI is represented by a bi-quadratic NURBS surface. Its control points and weights are listed in Tables 8 and 9. The knot vectors along u -, and v -directions are, respectively,

$$\begin{aligned} &0000.5111, \\ &0001111. \end{aligned}$$

Table 6: Control points of the cubic B-spline solid in Example III

i	j	$B_{i,j,1}$	$B_{i,j,2}$	$B_{i,j,3}$	$B_{i,j,4}$
1	1	(0,0,0)	(0,0,1/3)	(0,0,2/3)	(0,0,1)
1	2	(0,1/3,0)	(0,1/3,1/3)	(0,1/3,2/3)	(0,1/3,1)
1	3	(0,2/3,0)	(0,2/3,1/3)	(0,2/3,2/3)	(0,2/3,1)
1	4	(0,1,0)	(0,1,1/3)	(0,1,2/3)	(0,1,1)
2	1	(1/3,0,0)	(1/3,0,1/3)	(1/3,0,2/3)	(1/3,0,1)
2	2	(1/3,1/3,0)	(1/3,1/3,1/3)	(1/3,1/3,2/3)	(1/3,1/3,1)
2	3	(1/3,2/3,0)	(1/3,2/3,1/3)	(1/3,2/3,2/3)	(1/3,2/3,1)
2	4	(1/3,1,0)	(1/3,1,1/3)	(1/3,1,2/3)	(1/3,1,1)
3	1	(2/3,0,0)	(2/3,0,1/3)	(2/3,0,2/3)	(2/3,0,1)
3	2	(2/3,1/3,0)	(2/3,1/3,1/3)	(2/3,1/3,2/3)	(2/3,1/3,1)
3	3	(2/3,2/3,0)	(2/3,2/3,1/3)	(2/3,2/3,2/3)	(2/3,2/3,1)
3	4	(2/3,1,0)	(2/3,1,1/3)	(2/3,1,2/3)	(2/3,1,1)
4	1	(1,0,0)	(1,0,1/3)	(1,0,2/3)	(1,0,1)
4	2	(1,1/3,0)	(1,1/3,1/3)	(1,1/3,2/3)	(1,1/3,1)
4	3	(1,2/3,0)	(1,2/3,1/3)	(1,2/3,2/3)	(1,2/3,1)
4	4	(1,1,0)	(1,1,1/3)	(1,1,2/3)	(1,1,1)

Table 7: Control points of the cubic B-spline patch in Example IV.

i	$B_{i,1}$	$B_{i,2}$	$B_{i,3}$	$B_{i,4}$
1	(-5.0, -1.0)	(-1.67, -1.0)	(1.67, -1.0)	(5.0, -1.0)
2	(-5.0, -0.34)	(-1.67, -0.34)	(1.67, -0.34)	(5.0, -0.34)
3	(-5.0, 0.34)	(-1.67, 0.34)	(1.67, 0.34)	(5.0, 0.34)
4	(-5.0, 1.0)	(-1.67, 1.0)	(1.67, 1.0)	(5.0, 1.0)

Table 8: Control points of the physical domain of frame corner.

i	$B_{i,1}$	$B_{i,2}$	$B_{i,3}$	$B_{i,4}$
1	(-4, 0)	(-4, -4)	(-4, -4)	(0, -4)
2	(-2.5, 0)	(-2.5, -1.5)	(-1.5, -2.5)	(0, -2.5)
3	(-1, 0)	(-1, $-\sqrt{3}/3$)	($-\sqrt{3}$, -1)	(0, -1)

Table 9: Weights of the physical domain of frame corner.

i	$B_{i,1}$	$B_{i,2}$	$B_{i,3}$	$B_{i,4}$
1	1	1	1	1
2	1	1	1	1
3	1	$\sqrt{3}/2$	$\sqrt{3}/2$	1

A6: Proof to formula (18) in Theorem 2

Proof: We only show the theorem in the two-dimensional case. The proof for the one- and three-dimensional cases is similar.

In the two-dimensional case, suppose the tensor product NURBS function $T_r(u, v)$ of degree

$l_u \times l_v$ is defined on the knot sequences

$$\begin{aligned} & \underbrace{\{u_0, u_0, \dots, u_0, u_1, \dots, u_{n_u-1}, u_{n_u}, u_{n_u}, \dots, u_{n_u}\}}_{l_u+1}, \\ & \underbrace{\{v_0, v_0, \dots, v_0, v_1, \dots, v_{n_v-1}, v_{n_v}, v_{n_v}, \dots, v_{n_v}\}}_{l_v+1}. \end{aligned} \quad (31)$$

Then the corresponding knot grid is

$$\mathcal{T}^h = \{[u_i, u_{i+1}] \times [v_j, v_{j+1}], i = 0, 1, \dots, n_u - 1, j = 0, 1, \dots, n_v - 1\}. \quad (32)$$

Denote

$$R(u, v) = (\mathcal{DT}(u, v) - \mathcal{DT}_r(u, v))^2, (u, v) \in [u_0, u_{n_u}] \times [v_0, v_{n_v}].$$

Note that $T_r(u, v)$ is generated by least-squares fitting the values of $\mathcal{DT}(u, v)$ at the collocation points $\boldsymbol{\vartheta}_k = (\eta_k, \xi_k)$, i.e., $\mathcal{DT}(\boldsymbol{\vartheta}_k)$, $k = 1, 2, \dots, D$, ($D \geq n_u n_v$). And suppose the fitting error is

$$e_h = \sum_{k=1}^D R(\boldsymbol{\vartheta}_k) = \sum_{k=1}^D (\mathcal{DT}(\boldsymbol{\vartheta}_k) - \mathcal{DT}_r(\boldsymbol{\vartheta}_k))^2. \quad (33)$$

First, based on Lemma 1, the numerical solution $T_r(u, v)$ and the approximate differential operator $\mathcal{DT}_r(u, v)$ have the same knot intervals,

$$[u_i, u_{i+1}] \times [v_j, v_{j+1}], i = 0, 1, \dots, n_u - 1, j = 0, 1, \dots, n_v - 1.$$

Now, consider the error between $\mathcal{DT}(u, v)$ and $\mathcal{DT}_r(u, v)$ in the L^2 norm,

$$\|\mathcal{DT}(u, v) - \mathcal{DT}_r(u, v)\|_{L^2}^2 = \int_{v_0}^{v_{n_v}} \int_{u_0}^{u_{n_u}} R(u, v) dudv = \sum_{j=0}^{n_v-1} \sum_{i=0}^{n_u-1} \int_{v_j}^{v_{j+1}} \int_{u_i}^{u_{i+1}} R(u, v) dudv.$$

Since each knot interval $[u_i, u_{i+1}] \times [v_j, v_{j+1}]$ contains at least one collocation point, we suppose $\boldsymbol{\vartheta}_d = (\eta_d, \xi_d) \in [u_i, u_{i+1}] \times [v_j, v_{j+1}]$. Using the left and right rectangle integral formula repeatedly,

we get

$$\begin{aligned}
& \int_{v_j}^{v_{j+1}} \int_{u_i}^{u_{i+1}} R(u, v) dudv = \int_{v_j}^{v_{j+1}} dv \left(\int_{u_i}^{\eta_d} R(u, v) du + \int_{\eta_d}^{u_{i+1}} R(u, v) du \right) \\
& = \int_{v_j}^{v_{j+1}} \left((\eta_d - u_i)R(\eta_d, v) + (u_{i+1} - \eta_d)R(\eta_d, v) + (\eta_d - u_i)^2 \frac{R'_u(\mu_i^{(1)}(v), v)}{2} + (u_{i+1} - \eta_d)^2 \frac{R'_u(\mu_i^{(2)}(v), v)}{2} \right) dv \\
& = (u_{i+1} - u_i) \int_{v_j}^{v_{j+1}} R(\eta_d, v) dv + (\eta_d - u_i)^2 \int_{v_j}^{v_{j+1}} \frac{R'_u(\mu_i^{(1)}(v), v)}{2} dv + (u_{i+1} - \eta_d)^2 \int_{v_j}^{v_{j+1}} \frac{R'_u(\mu_i^{(2)}(v), v)}{2} dv \\
& = (u_{i+1} - u_i) \left((\xi_d - v_j)R(\eta_d, \xi_d) + (v_{j+1} - \xi_d)R(\eta_d, \xi_d) + (\xi_d - v_j)^2 \frac{R'_v(\eta_d, \omega_{ij}^{(1)})}{2} + (v_{j+1} - \xi_d)^2 \frac{R'_v(\eta_d, \omega_{ij}^{(2)})}{2} \right) \\
& \quad + (\eta_d - u_i)^2 \int_{v_j}^{v_{j+1}} \frac{R'_u(\mu_i^{(1)}(v), v)}{2} dv + (u_{i+1} - \eta_d)^2 \int_{v_j}^{v_{j+1}} \frac{R'_u(\mu_i^{(2)}(v), v)}{2} dv \\
& = (u_{i+1} - u_i)(v_{j+1} - v_j)R(\eta_d, \xi_d) + (u_{i+1} - u_i) \left((\xi_d - v_j)^2 \frac{R'_v(\eta_d, \omega_{ij}^{(1)})}{2} + (v_{j+1} - \xi_d)^2 \frac{R'_v(\eta_d, \omega_{ij}^{(2)})}{2} \right) \\
& \quad + (\eta_d - u_i)^2 \int_{v_j}^{v_{j+1}} \frac{R'_u(\mu_i^{(1)}(v), v)}{2} dv + (u_{i+1} - \eta_d)^2 \int_{v_j}^{v_{j+1}} \frac{R'_u(\mu_i^{(2)}(v), v)}{2} dv,
\end{aligned}$$

where $\mu_i^{(1)}(v), \mu_i^{(2)}(v) \in (u_i, u_{i+1})$ and $\omega_{ij}^{(1)}, \omega_{ij}^{(2)} \in (v_j, v_{j+1})$. By the mean value theorem of integral, there exist $(\bar{\mu}_{ij}^{(1)}, \bar{\omega}_{ij}^{(1)}), (\bar{\mu}_{ij}^{(2)}, \bar{\omega}_{ij}^{(2)}) \in [u_i, u_{i+1}] \times [v_j, v_{j+1}]$ such that

$$\begin{aligned}
& \int_{v_j}^{v_{j+1}} \frac{R'_u(\mu_i^{(1)}(v), v)}{2} dv = (v_{j+1} - v_j) \frac{R'_u(\bar{\mu}_{ij}^{(1)}, \bar{\omega}_{ij}^{(1)})}{2}, \text{ and} \\
& \int_{v_j}^{v_{j+1}} \frac{R'_u(\mu_i^{(2)}(v), v)}{2} dv = (v_{j+1} - v_j) \frac{R'_u(\bar{\mu}_{ij}^{(2)}, \bar{\omega}_{ij}^{(2)})}{2},
\end{aligned}$$

Therefore,

$$\begin{aligned}
& \int_{v_j}^{v_{j+1}} \int_{u_i}^{u_{i+1}} R(u, v) dudv = (u_{i+1} - u_i)(v_{j+1} - v_j)R(\eta_d, \xi_d) \\
& \quad + (u_{i+1} - u_i) \left((\xi_d - v_j)^2 \frac{R'_v(\eta_d, \omega_{ij}^{(1)})}{2} + (v_{j+1} - \xi_d)^2 \frac{R'_v(\eta_d, \omega_{ij}^{(2)})}{2} \right) \\
& \quad + (v_{j+1} - v_j) \left((\eta_d - u_i)^2 \frac{R'_u(\bar{\mu}_{ij}^{(1)}, \bar{\omega}_{ij}^{(1)})}{2} + (u_{i+1} - \eta_d)^2 \frac{R'_u(\bar{\mu}_{ij}^{(2)}, \bar{\omega}_{ij}^{(2)})}{2} \right).
\end{aligned}$$

Moreover, we denote $\Xi = [u_0, u_{n_u}] \times [v_0, v_{n_v}]$. It is easy to show that

$$\min_{(u,v) \in \Xi} |R'_v(u, v)| \leq \sum_{j=0}^{n_v-1} \sum_{i=0}^{n_u-1} \frac{(u_{i+1} - u_i)(v_{j+1} - v_j)}{(u_{n_u} - u_0)(v_{n_v} - v_0)} \frac{|R'_v(\eta_d, \omega_{ij}^{(1)})| + |R'_v(\eta_d, \omega_{ij}^{(2)})|}{2} \leq \max_{(u,v) \in \Xi} |R'_v(u, v)|,$$

$$\min_{(u,v) \in \Xi} |R'_u(u, v)| \leq \sum_{j=0}^{n_v-1} \sum_{i=0}^{n_u-1} \frac{(u_{i+1} - u_i)(v_{j+1} - v_j)}{(u_{n_u} - u_0)(v_{n_v} - v_0)} \frac{|R'_u(\bar{\mu}_{ij}^{(1)}, \bar{\omega}_{ij}^{(1)})| + |R'_u(\bar{\mu}_{ij}^{(2)}, \bar{\omega}_{ij}^{(2)})|}{2} \leq \max_{(u,v) \in \Xi} |R'_u(u, v)|.$$

And then, based on the intermediate value theorem, there exist $(\eta^{(1)}, \xi^{(1)}) \in \Xi$ and $(\eta^{(2)}, \xi^{(2)}) \in \Xi$, such that

$$\begin{aligned} |R'_v(\eta^{(1)}, \xi^{(1)})| &= \sum_{j=0}^{n_v-1} \sum_{i=0}^{n_u-1} \frac{(u_{i+1} - u_i)(v_{j+1} - v_j)}{(u_{n_u} - u_0)(v_{n_v} - v_0)} \frac{|R'_v(\eta_d, \omega_{ij}^{(1)})| + |R'_v(\eta_d, \omega_{ij}^{(2)})|}{2}, \\ |R'_u(\eta^{(2)}, \xi^{(2)})| &= \sum_{j=0}^{n_v-1} \sum_{i=0}^{n_u-1} \frac{(u_{i+1} - u_i)(v_{j+1} - v_j)}{(u_{n_u} - u_0)(v_{n_v} - v_0)} \frac{|R'_u(\bar{\mu}_{ij}^{(1)}, \bar{\omega}_{ij}^{(1)})| + |R'_u(\bar{\mu}_{ij}^{(2)}, \bar{\omega}_{ij}^{(2)})|}{2}. \end{aligned}$$

As a result,

$$\begin{aligned} \|\mathcal{D}T(u, v) - \mathcal{D}T_r(u, v)\|_{L^2}^2 &= \int_{v_0}^{v_{n_v}} \int_{u_0}^{u_{n_u}} R(u, v) du dv = \sum_{j=0}^{n_v-1} \sum_{i=0}^{n_u-1} \int_{v_j}^{v_{j+1}} \int_{u_i}^{u_{i+1}} R(u, v) du dv \\ &= \sum_{j=0}^{n_v-1} \sum_{i=0}^{n_u-1} (u_{i+1} - u_i)(v_{j+1} - v_j) R(\eta_d, \xi_d) \\ &\quad + \sum_{j=0}^{n_v-1} \sum_{i=0}^{n_u-1} (u_{i+1} - u_i) \left((\xi_d - v_j)^2 \frac{R'_v(\eta_d, \omega_{ij}^{(1)})}{2} + (v_{j+1} - \xi_d)^2 \frac{R'_v(\eta_d, \omega_{ij}^{(2)})}{2} \right) \\ &\quad + \sum_{j=0}^{n_v-1} \sum_{i=0}^{n_u-1} (v_{j+1} - v_j) \left((\eta_d - u_i)^2 \frac{R'_u(\bar{\mu}_{ij}^{(1)}, \bar{\omega}_{ij}^{(1)})}{2} + (u_{i+1} - \eta_d)^2 \frac{R'_u(\bar{\mu}_{ij}^{(2)}, \bar{\omega}_{ij}^{(2)})}{2} \right) \\ &\leq h^2 \sum_{d=1}^D R(\eta_d, \xi_d) + h \sum_{j=0}^{n_v-1} \sum_{i=0}^{n_u-1} (u_{i+1} - u_i)(v_{j+1} - v_j) \frac{|R'_v(\eta_d, \omega_{ij}^{(1)})| + |R'_v(\eta_d, \omega_{ij}^{(2)})|}{2} \\ &\quad + h \sum_{j=0}^{n_v-1} \sum_{i=0}^{n_u-1} (u_{i+1} - u_i)(v_{j+1} - v_j) \frac{|R'_u(\bar{\mu}_{ij}^{(1)}, \bar{\omega}_{ij}^{(1)})| + |R'_u(\bar{\mu}_{ij}^{(2)}, \bar{\omega}_{ij}^{(2)})|}{2} \\ &= h^2 e_h + h(u_{n_u} - u_0)(v_{n_v} - v_0) \left(|R'_v(\eta^{(1)}, \xi^{(1)})| + |R'_u(\eta^{(2)}, \xi^{(2)})| \right) \\ &< h^2 \bar{M} + h(u_{n_u} - u_0)(v_{n_v} - v_0) \left(|R'_v(\eta^{(1)}, \xi^{(1)})| + |R'_u(\eta^{(2)}, \xi^{(2)})| \right). \end{aligned}$$

On the other hand, since the degrees of u and v in $T_r(u, v)$ are both larger than the maximum orders of the partial derivatives to u and v appearing in \mathcal{D} (refer to (1)), respectively, similar as the one-dimensional case, $R'_u(u, v)$ and $R'_v(u, v)$ are both continuous, and then bounded on $\Omega \cup \partial\Omega$, i.e.,

$$|R'_v(\eta^{(1)}, \xi^{(1)})| \leq \hat{M}, \text{ and, } |R'_u(\eta^{(2)}, \xi^{(2)})| \leq \hat{M},$$

where \hat{M} is a positive constant.

In conclusion,

$$\|\mathcal{D}T(u, v) - \mathcal{D}T_r(u, v)\|_{L^2}^2 \leq h^2 \bar{M} + 2h(u_{n_u} - u_0)(v_{n_v} - v_0) \hat{M},$$

and Theorem 2 is proved. \square

References

- [1] T.J.R. Hughes, J.A. Cottrell, and Y. Bazilevs. Isogeometric analysis: Cad, finite elements, nurbs, exact geometry and mesh refinement. *Computer methods in applied mechanics and engineering*, 194(39):4135–4195, 2005.
- [2] F. Auricchio, L. Beirão da Veiga, TJR Hughes, A. Reali, and G. Sangalli. Isogeometric collocation methods. *Mathematical Models and Methods in Applied Sciences*, 20(11):2075–2107, 2010.
- [3] Xiong Zhang, Xiao-Hu Liu, Kang-Zu Song, and Ming-Wan Lu. Least-squares collocation meshless method. *International Journal for Numerical Methods in Engineering*, 51(9):1089–1100, 2001.
- [4] Bo-Nan Jiang. Least-squares meshfree collocation method. *International Journal of Computational Methods*, 9(02), 2012.
- [5] Do Wan Kim and Yongsik Kim. Point collocation methods using the fast moving least-square reproducing kernel approximation. *International Journal for Numerical Methods in Engineering*, 56(10):1445–1464, 2003.
- [6] YJ Dai, XH Wu, and WQ Tao. Weighted least-squares collocation method (wlscm) for 2-d and 3-d heat conduction problems in irregular domains. *Numerical Heat Transfer, Part B: Fundamentals*, 59(6):473–494, 2011.
- [7] MH Afshar, M Lashckarbolok, and G Shobeyri. Collocated discrete least squares meshless (cdlsm) method for the solution of transient and steady-state hyperbolic problems. *International journal for numerical methods in fluids*, 60(10):1055–1078, 2009.
- [8] Bernard BT Kee, GR Liu, and C Lu. A least-square radial point collocation method for adaptive analysis in linear elasticity. *Engineering analysis with boundary elements*, 32(6):440–460, 2008.
- [9] T Rabczuk, T Belytschko, and SP Xiao. Stable particle methods based on lagrangian kernels. *Computer methods in applied mechanics and engineering*, 193(12):1035–1063, 2004.
- [10] T Rabczuk and T Belytschko. Cracking particles: a simplified meshfree method for arbitrary evolving cracks. *International Journal for Numerical Methods in Engineering*, 61(13):2316–2343, 2004.
- [11] T Rabczuk and T Belytschko. A three-dimensional large deformation meshfree method for arbitrary evolving cracks. *Computer Methods in Applied Mechanics and Engineering*, 196(29):2777–2799, 2007.
- [12] L.A. Piegl and W. Tiller. *The NURBS book*. Springer Verlag, 1997.
- [13] C. De Boor. *A practical guide to splines*, volume 27. Springer Verlag, 2001.
- [14] Yongjie Zhang, Wenyan Wang, and Thomas JR Hughes. Solid t-spline construction from boundary representations for genus-zero geometry. *Computer Methods in Applied Mechanics and Engineering*, 249:185–197, 2012.
- [15] E. Cohen, T. Martin, RM Kirby, T. Lyche, and RF Riesenfeld. Analysis-aware modeling: Understanding quality considerations in modeling for isogeometric analysis. *Computer Methods in Applied Mechanics and Engineering*, 199(5):334–356, 2010.
- [16] Y. Bazilevs, VM Calo, JA Cottrell, JA Evans, TJR Hughes, S. Lipton, MA Scott, and TW Sederberg. Isogeometric analysis using t-splines. *Computer Methods in Applied Mechanics and Engineering*, 199(5):229–263, 2010.
- [17] M.R. Dörfel, B. Jüttler, and B. Simeon. Adaptive isogeometric analysis by local h -refinement with t-splines. *Computer methods in applied mechanics and engineering*, 199(5):264–275, 2010.
- [18] H.J. Kim, Y.D. Seo, and S.K. Youn. Isogeometric analysis for trimmed cad surfaces. *Computer Methods in Applied Mechanics and Engineering*, 198(37):2982–2995, 2009.
- [19] D. Burkhart, B. Hamann, and G. Umlauf. Iso-geometric finite element analysis based on catmull-clark subdivision solids. In *Computer Graphics Forum*, volume 29, pages 1575–1584. Wiley Online Library, 2010.
- [20] Hendrik Speleers, Carla Manni, Francesca Pelosi, and M Lucia Sampoli. Isogeometric analysis with powell–sabin splines for advection–diffusion–reaction problems. *Computer Methods in Applied Mechanics and Engineering*, 221:132–148, 2012.
- [21] Noah Jaxon and Xiaoping Qian. Isogeometric analysis on triangulations. *Computer-Aided Design*, 46:45–57, 2014.
- [22] F. Auricchio, L. Beirão da Veiga, A. Buffa, C. Lovadina, A. Reali, and G. Sangalli. A fully locking-free isogeometric approach for plane linear elasticity problems: a stream function formulation. *Computer methods in applied mechanics and engineering*, 197(1):160–172, 2007.
- [23] T. Elguedj, Y. Bazilevs, VM Calo, and TJR Hughes. \bar{B} and \bar{F} projection methods for nearly incompressible linear and non-linear elasticity and plasticity using higher-order nurbs elements. *Comput. Methods Appl. Mech. Engrg.*, 197:2732–2762, 2008.
- [24] JA Cottrell, A. Reali, Y. Bazilevs, and TJR Hughes. Isogeometric analysis of structural vibrations. *Computer methods in applied mechanics and engineering*, 195(41):5257–5296, 2006.
- [25] T.J.R. Hughes, A. Reali, and G. Sangalli. Duality and unified analysis of discrete approximations in structural dynamics and wave propagation: Comparison of p -method finite elements with k -method nurbs. *Computer methods in applied mechanics and engineering*, 197(49):4104–4124, 2008.
- [26] W.A. Wall, M.A. Frenzel, and C. Cyron. Isogeometric structural shape optimization. *Computer Methods in Applied Mechanics and Engineering*, 197(33):2976–2988, 2008.
- [27] Y. Bazilevs, VM Calo, T.J.R. Hughes, and Y. Zhang. Isogeometric fluid-structure interaction: theory, algorithms, and computations. *Computational Mechanics*, 43(1):3–37, 2008.

- [28] Y. Bazilevs, VM Calo, Y. Zhang, and T.J.R. Hughes. Isogeometric fluid–structure interaction analysis with applications to arterial blood flow. *Computational Mechanics*, 38(4):310–322, 2006.
- [29] Y. Bazilevs, JR Gohean, TJR Hughes, RD Moser, and Y. Zhang. Patient-specific isogeometric fluid–structure interaction analysis of thoracic aortic blood flow due to implantation of the jarvik 2000 left ventricular assist device. *Computer Methods in Applied Mechanics and Engineering*, 198(45):3534–3550, 2009.
- [30] Y. Bazilevs, L Beirão da Veiga, JA Cottrell, TJR Hughes, and G. Sangalli. Isogeometric analysis: approximation, stability and error estimates for h-refined meshes. *Mathematical Models and Methods in Applied Sciences*, 16(07):1031–1090, 2006.
- [31] JA Cottrell, TJR Hughes, and A. Reali. Studies of refinement and continuity in isogeometric structural analysis. *Computer methods in applied mechanics and engineering*, 196(41):4160–4183, 2007.
- [32] T.J.R. Hughes, A. Reali, and G. Sangalli. Efficient quadrature for nurbs-based isogeometric analysis. *Computer methods in applied mechanics and engineering*, 199(5):301–313, 2010.
- [33] M. Aigner, C. Heinrich, B. Jüttler, E. Pilgerstorfer, B. Simeon, and A. Vuong. Swept volume parameterization for isogeometric analysis. *Mathematics of Surfaces XIII*, pages 19–44, 2009.
- [34] G. Xu, B. Mourrain, R. Duvigneau, and A. Galligo. Optimal analysis-aware parameterization of computational domain in 3d isogeometric analysis. *Computer-Aided Design*, 45(4):812–821, 2013.
- [35] Marco Donatelli, Carlo Garoni, Carla Manni, Stefano Serra-Capizzano, and Hendrik Speleers. Robust and optimal multi-iterative techniques for IgA galerkin linear systems. *Computer Methods in Applied Mechanics and Engineering*, 284:230–264, 2015.
- [36] Marco Donatelli, Carlo Garoni, Carla Manni, Stefano Serra-Capizzano, and Hendrik Speleers. Robust and optimal multi-iterative techniques for IgA collocation linear systems. *Computer Methods in Applied Mechanics and Engineering*, 284:1120–1146, 2015.
- [37] J.A. Cottrell, T.J.R. Hughes, and Y. Bazilevs. *Isogeometric analysis: toward integration of CAD and FEA*. Wiley, 2009.
- [38] Dominik Schillinger, John A Evans, Alessandro Reali, Michael A Scott, and Thomas JR Hughes. Isogeometric collocation: Cost comparison with galerkin methods and extension to adaptive hierarchical nurbs discretizations. *Computer Methods in Applied Mechanics and Engineering*, 267:170–232, 2013.
- [39] Hongwei Lin, Qianqian Hu, and Yunyang Xiong. Consistency and convergence properties of the isogeometric collocation method. *Computer Methods in Applied Mechanics and Engineering*, 267:471–486, 2013.
- [40] Cosmin Anitescu, Yue Jia, Yongjie Jessica Zhang, and Timon Rabczuk. An isogeometric collocation method using superconvergent points. *Computer Methods in Applied Mechanics and Engineering*, 284:1073–1097, 2015.
- [41] Monica Montardini, Giancarlo Sangalli, and Lorenzo Tamellini. Optimal-order isogeometric collocation at galerkin superconvergent points. *Computer Methods in Applied Mechanics and Engineering*, 2016.
- [42] Hector Gomez and Laura De Lorenzis. The variational collocation method. *Computer Methods in Applied Mechanics and Engineering*, 309:152–181, 2016.
- [43] Hugo Casquero, Lei Liu, Yongjie Zhang, Alessandro Reali, and Hector Gomez. Isogeometric collocation using analysis-suitable T-splines of arbitrary degree. *Computer Methods in Applied Mechanics and Engineering*, 301:164–186, 2016.
- [44] F Auricchio, L Beirão da Veiga, TJR Hughes, A Reali, and G Sangalli. Isogeometric collocation for elastostatics and explicit dynamics. *Computer methods in applied mechanics and engineering*, 249:2–14, 2012.
- [45] L Beirão da Veiga, C Lovadina, and A Reali. Avoiding shear locking for the timoshenko beam problem via isogeometric collocation methods. *Computer methods in applied mechanics and engineering*, 241:38–51, 2012.
- [46] F Auricchio, L Beirão da Veiga, J Kiendl, C Lovadina, and A Reali. Locking-free isogeometric collocation methods for spatial timoshenko rods. *Computer Methods in Applied Mechanics and Engineering*, 263(15):113–126, 2013.
- [47] Giuseppe Balduzzi, Simone Morganti, Ferdinando Auricchio, and Alessandro Reali. Non-prismatic timoshenko-like beam model: Numerical solution via isogeometric collocation. *Computers & Mathematics with Applications*, in press, 2017.
- [48] G.S. Pavan and K.S. Nanjunda Rao. Bending analysis of laminated composite plates using isogeometric collocation method. *Composite Structures*, in press, 2017.
- [49] Gene H Golub and Charles F van Van Loan. Matrix computations (johns hopkins studies in mathematical sciences). 1996.
- [50] A Yu Shadrin. The l_∞ -norm of the l_2 -spline projector is bounded independently of the knot sequence: A proof of de boor’s conjecture. *Acta Mathematica*, 187(1):59–137, 2001.
- [51] Markus Passenbrunner and Joscha Prochno. On almost everywhere convergence of tensor product spline projections. *arXiv preprint arXiv:1310.6505*, 2013.
- [52] Pavel Solin. *Partial differential equations and the finite element method*. Wiley-Interscience, 2006.